MIT Open Access Articles

Quantifying and Interpreting Striations in a Subtropical Gyre: A Spectral Perspective

Massachusetts Institute of Technology

Quantifying and Interpreting Striations in a Subtropical Gyre: A Spectral Perspective

RU CHEN*

Massachusetts Institute of Technology–Woods Hole Oceanographic Institution Joint Program, Cambridge, Massachusetts

GLENN R. FLIERL

Massachusetts Institute of Technology, Cambridge, Massachusetts

CARL WUNSCH

Massachusetts Institute of Technology, and Harvard University, Cambridge, Massachusetts

ABSTRACT

The amplitude, origin, and direction of striations in the subtropical gyre are investigated using simulated and analytical multidimensional spectra. Striations, defined as banded structures in the low-frequency motions, account for a noticeable percentage of zonal velocity variability in the east North Pacific (ENP: 25°–42°N, 150°–130°W) and central North Pacific (CNP: 10°–22°N, 132°E–162°W) regions in an eddying global ocean model. Thus, they likely are nonnegligible in mixing and transport processes. Striations in the ENP region are nonzonal and are embedded in the nonzonal gyre flow, whereas striations in the CNP region are more zonal, as are the mean gyre flows. An idealized 1.5-layer model shows the gyre flow partially determines their directions, which qualitatively resemble those in the global eddying model. In the linear limit, structures are quasi-stationary (frequency $\omega \to 0$) linear Rossby waves and the gyre flow influences the direction by influencing the nature of the zero Rossby wave frequency curve. In the nonlinear regime, striations are consistent with the nondispersively propagating eddies, whose low-frequency component has banded structures. The gyre flow influences the striation direction by changing the eddy propagation direction. Their origin in the nonlinear regime is consistent with the existence of a nondispersive line in the frequency–wavenumber spectra. This study does not exclude other striation mechanisms from literature, considering that the interpretations here are based on an idealized model and only from a spectral perspective.

1. Introduction

As ocean modeling and observation techniques enter the eddy-resolving regime, a new feature of the oceanic circulation emerges: the temporal average of some oceanic variables, such as zonal velocity, has banded structures. These banded structures have been identified from eddying numerical models (Cox 1987; Galperin et al. 2004; Nakano and Hasumi 2005; Richards et al. 2006), the satellite altimetric data (Maximenko et al. 2005), and the in situ XBT/float data (Maximenko et al. 2008). Previous studies term these features "jets" or "striations." They are pervasive, and they contribute to the transport of heat, tracers, chemicals, and biota (e.g., Baldwin et al. 2007; Kamenkovich et al. 2009). Although a number of recent studies exist, many striation aspects are still under debate, including their amplitudes and origins.

Oceanic variability contains much more kinetic energy than the long-term time-mean circulation (Ferrari and Wunsch 2009), and part of it is banded (Maximenko et al. 2005). What fraction of the energy is banded and what the consequences are of these special structures for the larger scales, if any, remain unknown. In the regions away from the Southern Ocean, bands are visible only in the temporally averaged flow field, not in flow snapshots (Thompson 2010; Berloff et al. 2011). Thus, many

* Current affiliation: Scripps Institution of Oceanography, University of California, San Diego, La Jolla, California.

Corresponding author address: Ru Chen, Scripps Institution of Oceanography, University of California, San Diego, 8622 Kennel Way, La Jolla, CA 92037.
E-mail: ruchen@alum.mit.edu

previous studies explore striations by temporally averaging the flow field; averaging intervals range from weeks to years, depending on the record length and the research goal (e.g., Maximenko et al. 2005; Richards et al. 2006; van Sebille et al. 2011). Amplitudes generally decrease as the averaging length increases, carrying implications about time scales and inferred properties (e.g., Buckingham and Cornillon 2013).

One origin hypothesis is that they are "Rhines jets," which arise from the arrest of the inverse cascade by the beta effect (Rhines 1975; Thompson 2010; Boland et al. 2012). Alternatively, Schlax and Chelton (2008) proposed that apparent banded structures could be a purely kinematic result of propagating vortices. They found that temporally averaging westward-propagating vortices, with statistical characteristics similar to altimeter observations, produced banded features because cyclones (anticyclones) contribute westward (eastward) flow at the northern edge of the track and eastward (westward) flow at the southern edge of the track. We term this hypothesis the "vortex propagation mechanism." Other formation mechanisms include, but are not limited to, convergence of eddy momentum fluxes in baroclinically unstable regions (Panetta 1993), nonlinear interactions of resonant basin modes (Berloff 2005), radiating instability of the eastern boundary current (Hristova et al. 2008; Wang et al. 2013), stationary Rossby waves (Maximenko et al. 2008), beta plumes (Afanasyev et al. 2012), and zonostrophic instability (Srinivasan and Young 2012).

The large-scale wind-driven flow, usually ignored in the mechanisms summarized above, further complicates understanding the origin and characteristics of striations. Previous studies found that they can be generated in two-layer basin models forced by double-gyre winds, and their origin is interpreted using some of the above concepts (Tanaka and Akitomo 2010; O'Reilly et al. 2012). However, these studies did not explicitly examine the influence of the gyre mean flow.

Here, the intention is to quantify and interpret striations in frequency–wavenumber space in the presence of gyre flows. Goals are twofold: 1) to estimate the percentage of zonal velocity variability and eddy energy associated with striations in the North Pacific Subtropical Gyre using a constrained eddy-permitting state estimate (section 3) and 2) to investigate the effect of a subtropical gyre on the origin and properties of striations in an idealized model (sections 4 and 5). In addition, we provide a basic description of striations from the Estimating the Circulation and Climate of the Ocean, phase 2, high-resolution global-ocean and sea ice data synthesis (ECCO2) in section 2 and conclude the paper in section 6.

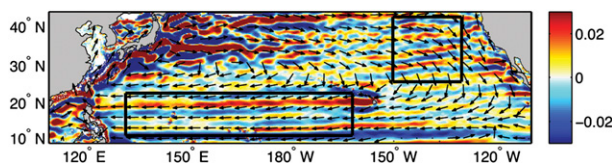FIG. 1. The time-mean small-scale zonal velocity (color; $m s^{-1}$) and the direction of the large-scale time-mean velocity (vectors) on the time-mean $1025.6 \, kg \, m^{-3}$ isopycnal from the ECCO2 state estimate. Black boxes denote the CNP and ENP regions. Here, time-mean denotes the temporal average over the years 1992–2007, large scale means the $4° \times 4°$ running average, and small scale is the deviation from the large scales.

2. Basic description of striations in the ECCO2 state estimate

The goal of the Estimating the Circulation and Climate of the Ocean (ECCO) project is to produce estimates of the global, time-varying ocean circulation that are consistent with diverse global datasets and that, in contrast with "reanalysis-like" products, satisfy basic energy, water, and so on, conservation requirements [see Wunsch and Heimbach (2013) for a summary] and whose time evolution is fully consistent with exactly known general circulation model equations. This study uses one of the products from the project: a global, eddy-permitting state estimate constrained by observations through the Green function approach (e.g., Menemenlis et al. 2008; Chen 2013).[1]

A visual depiction of striations in the time-mean zonal velocity field from the state estimate can be seen in Fig. 1. There the gyre flow is the large-scale time-mean circulation on a representative isopycnal in the upper North Pacific Ocean. Banded structures are pervasive in the domain and they are particularly conspicuous in the Kuroshio Extension, the central North Pacific (CNP; 10°–22°N, 132°E–162°W), and the east North Pacific (ENP; 25°–42°N, 150°–130°W) regions. This study focuses on the CNP and ENP regions, as the gyre flow in these regions varies slowly spatially, making it possible to use a simple dynamical framework.

Visible bands in the CNP region, one with zonal gyre flow, are also zonal, but those in the ENP region tilt southwestward in the nonzonal gyre flow. The latter character has been noticed before (e.g., Maximenko et al. 2008; Centurioni et al. 2008), and a goal here is to understand how the large-scale flow field influences bands.

Striations in these two regions roughly align with eddy trajectories (Fig. 2), calculated from

---

[1] The model output used in this study is the available 3-day-averaged fields, interpolated from the cube sphere grids onto uniform $\frac{1}{4}° \times \frac{1}{4}°$ grids during the years 1992–2007.
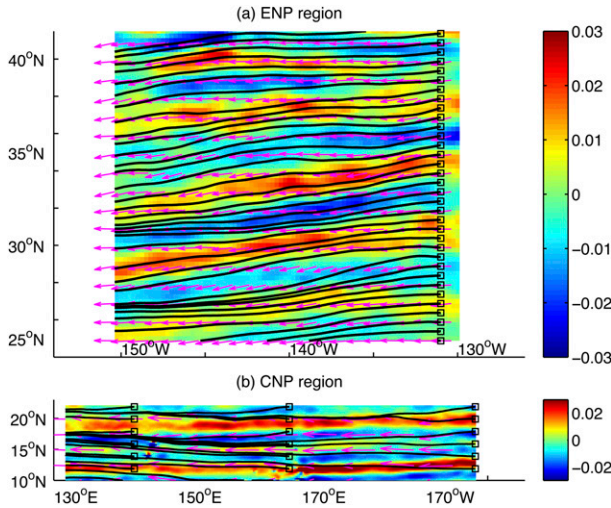
FIG. 2. The time-mean small-scale zonal velocity (color, m s^{-1}) as shown in Fig. 1 and the eddy trajectories (black lines) starting from the black boxes in the (a) ENP and the (b) CNP regions at 300 m. Vectors denote the direction of the eddy propagation velocities, diagnosed using the method in appendix A. The ECCO2 state estimate is used for this diagnosis.

$$\frac{d}{dt}x_{eddy}(t) = C_x(x_{eddy}, y_{eddy}),$$
$$\frac{d}{dt}y_{eddy}(t) = C_y(x_{eddy}, y_{eddy}), \quad (1)$$

with the initial condition $x_{eddy}(0) = x_0$ and $y_{eddy}(0) = y_0$. The quantities $x_{eddy}(t)$ and $y_{eddy}(t)$ are the eddy position at time t. The variables C_x and C_y are the zonal and meridional components of eddy propagation velocity, calculated from the ECCO2 state estimate using the method in appendix A. Recent observations show that the effect of ocean currents on eddy propagation velocity in the mid- and high latitudes is large (Fu 2009).

3. Percentage of variability associated with striations

a. A definition

Because striations are mostly studied using the temporally averaged fields, they are here defined as banded structures in the low-frequency motions, consistent with most of the existing literature. To separate low- and high-frequency motions, consider as an example the zonal velocity anomaly[2] $u'(x, y, z, t)$. Define the normalized wavenumber spectrum of $u'(x, y, z, t)$ at frequency ω in an oceanic region as

---

[2] Anomaly hereinafter denotes the deviation of the variable from its time mean, which in the ECCO2 state estimate is 16 yr.

$$S_{u'}^N(k, l, \omega, z) = \frac{S_{u'}(k, l, \omega, z)}{[S_{u'}(k, l, \omega, z)]_{max}}. \quad (2)$$

Here, $S_{u'}(k, l, \omega, z)$ denotes the frequency–wavenumber spectrum of u', that is,

$$S_{u'}(k, l, \omega, z) = \langle|\widehat{u'}(k, l, \omega, z)|^2\rangle, \quad (3)$$

where the hat denotes the three-dimensional Fourier transform, k is the zonal wavenumber, l is the meridional wavenumber, and ω is the frequency. Following Wortham and Wunsch (2014), $\langle \cdot \rangle$ in this section denotes averaging over three neighboring frequency–wavenumber bands. In the next section, $\langle \cdot \rangle$ denotes averaging over three neighboring frequency–wavenumber bands and then averaging over 10 realizations. Here, $[S_{u'}(k, l, \omega, z)]_{max}$ is the maximum value of $S_{u'}(k, l, \omega, z)$ in the available wavenumber space at frequency ω and depth z. Define (k_n, l_n) as the wavenumbers where $S_{u'}^N(k, l, \omega, z)$ is larger than an arbitrarily chosen value (0.2) at frequency ω and depth z. The optimum ellipse is defined as the smallest one for which all the (k_n, l_n) are inside (Fig. 3). If the ratio between the major and minor axes of that ellipse is large, eddy structures are elongated along the minor axis, and thus banded structures dominate in the zonal velocity field at frequency ω (Fig. 3). Our arbitrary criterion is that if the ratio is larger than three, the optimum ellipse is "narrow" and ω is one of the frequencies with striations. As shown in the next section, the wavenumber spectra of zonal velocity in the ocean generally become more isotropic as the frequency increases; thus, the ratio decreases as frequency increases. A separation frequency between low- and high-frequency motions Ω_S is defined as the highest frequency where all the ratios at frequencies lower than Ω_S are larger than three.

b. Results

1) ZONAL VELOCITY AND ZONAL GEOSTROPHIC VELOCITY

The percentage of zonal velocity variability associated with striations is defined as

$$\text{percentage}(z) = \frac{\int_{-\Omega_S}^{\Omega_S}\left[\iint_{D_{kl}(\omega,z)} S_{u'}(k, l, \omega, z)\, dk\, dl\right] d\omega}{\iiint_{\mathcal{V}} S_{u'}(k, l, \omega, z)\, dk\, dl\, d\omega}, \quad (4)$$

where $D_{kl}(\omega, z)$ represents the wavenumber space inside the optimum ellipse at frequency ω and depth z, and $\mathcal{V}$ denotes the entire available three-dimensional frequency–wavenumber space. This definition can also

(a) Narrow optimum ellipse

(b) Elongated eddies

(c) Wide optimum ellipse

(d) Isotropic eddies

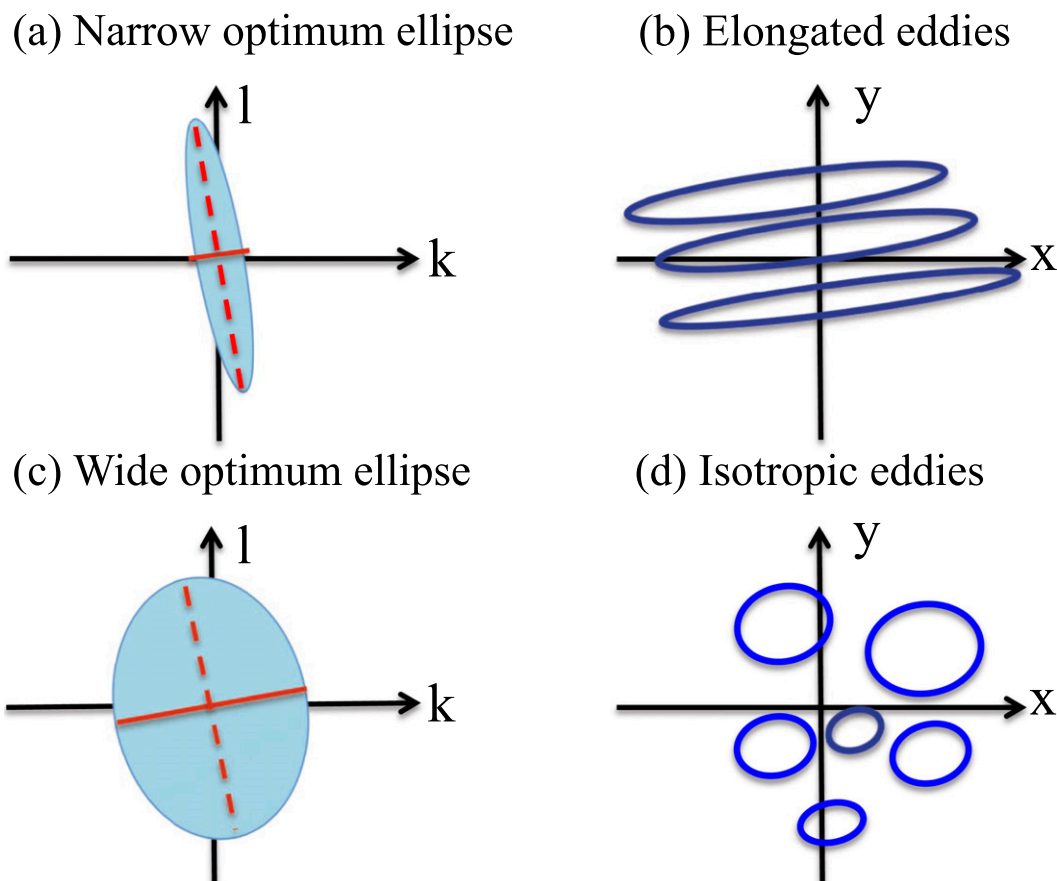FIG. 3. Schematics illustrating how we determine the separation frequency Ω_S. (a) If the optimum ellipse is very narrow, most variability is along the major axis (dashed red line), and (b) thus eddies are elongated in the direction of the minor axis (solid red line). (c) If the optimum ellipse is wide, the percentage of oceanic variability at all directions are comparable to each other, (d) eddies are more isotropic.

be used to calculate the percentage of striation structures in other variables (e.g., temperature). Results may be sensitive to the available record length and the resolution of wavenumbers and frequencies, but that element is not further explored here.

Using the procedure in section 3a, the separation frequency Ω_S for the surface zonal geostrophic velocity anomaly was obtained using

$$ u'_{s,\text{geo}}(x,y,z,t) = -\frac{g}{f}\frac{\partial \eta'(x,y,z,t)}{\partial y}, \qquad (5) $$

where f is the Coriolis parameter and $\eta'(x, y, z, t)$ is the deviation of sea surface height (SSH) from the time mean over the years 1992–2009.[3] The value $\Omega_S = 1/8.6$ cycle month^{-1} in the CNP region and $1/2.7$ cycle yr^{-1} in the ENP region. The frequency–wavenumber spectra

integrated over frequencies lower than Ω_S are much more anisotropic than those integrated over frequencies higher than Ω_S (Fig. 4). Banded structures are clearly visible in the eddy field with frequencies lower than Ω_S, but not in the eddy field at frequencies higher than Ω_S (e.g., Fig. 5).

Analysis of the altimetric data suggests that the percentage of the $u'_{s,\text{geo}}$ variability associated with striations is about 14% in the ENP region and 24% in the CNP region. In the ECCO2 state estimate in both regions, the percentage of striation zonal velocity variability varies little in the vertical between 300 and 1000 m (Fig. 6). Small vertical variation is consistent with the vertical coherence reported in previous studies (e.g., Richards et al. 2006; van Sebille et al. 2011). Vertically averaged percentages in this depth range are 14% in the ENP and 45% in the CNP region.

2) KINETIC ENERGY AND AVAILABLE POTENTIAL ENERGY

Define eddy kinetic energy (EKE) in the ECCO2 state estimate as

---

[3] We use the weekly SSH from altimetry smoothed and gridded at $1/4°$ spatial resolution (Dibarboure et al. 2009).
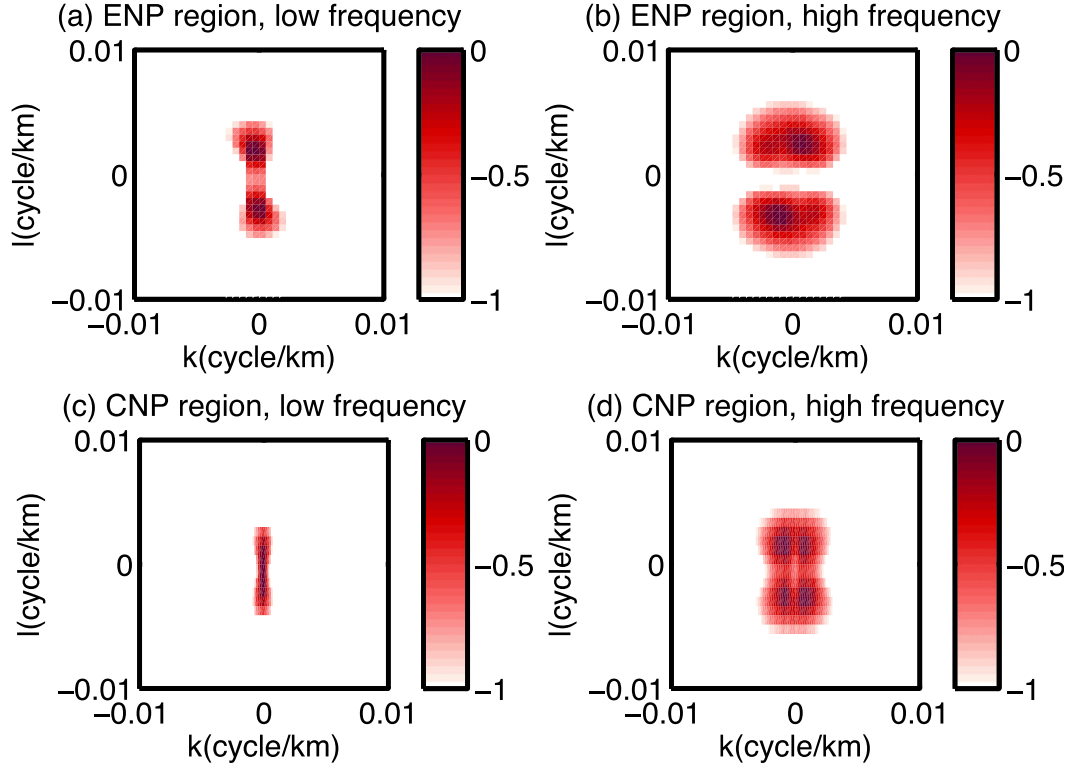
FIG. 4. Normalized wavenumber spectrum of the part of $u'_{s,\text{geo}}$ with frequency (a),(c) lower and (b),(d) higher than Ω_S in the two regions from the altimetric data. Scale of colorbars is logarithmic.

$$K_E(x,y,z,t) = \frac{1}{2}\rho_0(u'^2 + v'^2), \qquad (6)$$

where $v'(x,y,z,t)$ is meridional velocity anomaly, and ρ_0 is the constant reference density in the model ($1027.5\,\text{kg m}^{-3}$). Eddy available potential energy (EAPE) is defined as

$$P_E(x,y,z,t) = \frac{g^2}{2\rho_0 N^2(z)}\rho'^2, \qquad (7)$$

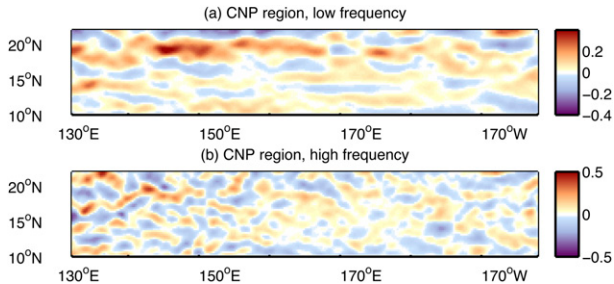where $\rho'(x,y,z,t)$ is the in situ density anomaly, g is gravity, and $N^2(z)$ is the global average time-mean

buoyancy frequency at depth z (Oort et al. 1989; Huang 2010; Storch et al. 2012; Chen 2013). The frequency–wavenumber spectra of EKE and EAPE are

$$S_{K_E}(k,l,\omega,z) = \frac{1}{2}\rho_0\langle|\widehat{u'}(k,l,\omega,z)|^2\rangle$$
$$+ \frac{1}{2}\rho_0\langle|\widehat{v'}(k,l,\omega,z)|^2\rangle, \qquad (8)$$

and

FIG. 5. Snapshots of the part of $u'_{s,\text{geo}}$ (m s^{-1}) with frequency (a) lower and (b) higher than Ω_S in the CNP region from the altimetric data. Corresponding figures for the ENP region are not shown for brevity.
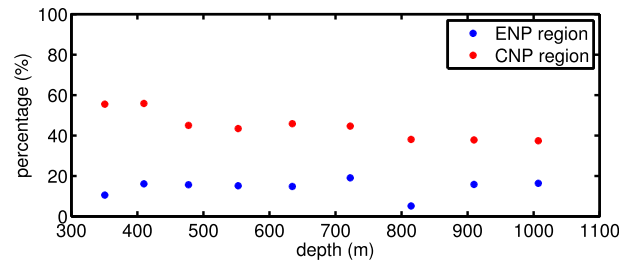
FIG. 6. The percentage of the zonal velocity variability associated with striations as a function of depth from the ECCO2 state estimate. Note that we choose to estimate the vertical structure of percentage in the depth range away from the mixed layer, in which the dynamics are very different from below, and away from bottom topography. Our method to obtain Ω_S does not apply well near bottom topography because of the difficulty in estimating the frequency–wavenumber spectrum in the area with lands.

$$S_{P_E}(k, l, \omega, z) = \frac{g^2}{2\rho_0 N^2(z)} \langle |\hat{\rho}'(k, l, \omega, z)|^2 \rangle. \quad (9)$$

From Eq. (4), with $S_{K_E}(k, l, \omega, z)$ and $S_{P_E}(k, l, \omega, z)$, the eddy energy associated with striations in the ECCO2 state estimate is found. At 300–1000 m in the CNP region, the vertically averaged percentages of striation EKE and EAPE are 21% and 32%. In the ENP region, however, the fractions in the state estimate are indistinguishable from zero. Differences in the fraction between the two regions are likely related to their differing frequency–wavenumber spectra, as characterized by Wortham (2013).

4. Effect of the gyre flow on idealized striations

Section 3 shows that striations are a noticeable component of oceanic motions and thus are potentially important in the energy cycle and mixing processes. As a useful step to understand these potential consequences of striations, their origin in the gyre flow is investigated next.

a. Model formulation

In eddy studies, 1.5-layer models have been widely used (e.g., McWilliams and Flierl 1979; Cushman-Roisin et al. 1990; Radko and Stern 1999; Jacob et al. 2002; Klocker et al. 2012). Transport properties, propagation speeds of nonlinear vortices, and the spectra in the nonlinear 1.5-layer model, at least qualitatively, resemble those from altimetry (e.g., Early et al. 2011). Next, we derive a 1.5-layer model explicitly including the gyre effect.

We start from the potential vorticity (PV) equation, as used in Cushman-Roisin et al. (1990):

$$\frac{\partial}{\partial t}q + J(\psi, q) = \mathcal{F}(x, y, t) - rq, \quad (10)$$

where J is the Jacobian operator, $\mathcal{F}(x, y, t)$ is the external forcing, and r is the friction coefficient. Here, q denotes PV $\nabla^2\psi - F_1\psi + \beta y$, where ψ is the streamfunction, F_1 is the squared inverse of the deformation radius, and β is the meridional gradient of the Coriolis parameter. As in Wang et al. (2013), we decompose the field into steady (overbar) and perturbation (prime) components:

$$\psi = \overline{\psi} + \psi', \quad \text{and}$$
$$q = \overline{q} + q' = (\nabla^2\overline{\psi} - F_1\overline{\psi} + \beta y) + (\nabla^2\psi' - F_1\psi'). \quad (11)$$

The basic state ($\overline{\psi}$ and $\overline{q}$) is forced by the steady forcing part and satisfies

$$J(\overline{\psi}, \overline{q}) = \overline{\mathcal{F}} - r\overline{q}. \quad (12)$$

Substituting Eqs. (11) and (12) into Eq. (10) leads to

$$\frac{\partial}{\partial t}q' + J(\overline{\psi} + \psi', q') + J(\psi', \overline{q}) = \mathcal{F}'(x, y, t) - rq'. \quad (13)$$

We define the steady-state gyre flow as $(U, V) = (-\overline{\psi}_y, \overline{\psi}_x)$, and assume that the steady-state flow varies slowly, and thus $\nabla^2\overline{\psi}$ is a negligible component of $\overline{q}$. Then, Eq. (13) is converted to the following, after ignoring primes for simplicity:

$$\left(\frac{\partial}{\partial t} + U\frac{\partial}{\partial x} + V\frac{\partial}{\partial y}\right)q + J(\psi, q) + J(\psi, Q) = \mathcal{F}(x, y, t) - rq, \quad (14)$$

where hereinafter ψ is the perturbation streamfunction, $q = \nabla^2\psi - F_1\psi$ denotes the perturbation PV, and $Q = \beta y + F_1(Uy - Vx)$ is the gyre-scale PV. Appendix B provides an alternative derivation based on the shallow-water model, which allows large spatial variation of layer thickness.

b. Experiment setup

Equation (14) is solved in a channel with north–south periodicity by means of a pseudospectral code. The channel model can be used because zonal boundary layers do not exist at the northern/southern boundaries of the channel and thus have no effect on striations. Zero normal flow boundary conditions are used on the western and eastern boundaries: $\beta = 2 \times 10^{-11}\,\mathrm{s}^{-1}\,\mathrm{m}^{-1}$ and $r = 3.5 \times 10^{-8}\,\mathrm{s}^{-1}$. The deformation radius is 50 km in a domain 8960 km wide and 5120 km long, approximately the size of the North Pacific. Numerical experiments are carried out on 256×256 grid points with a time step of ⅛ day.

The imposed mean flow (U, V) is a steady double gyre (Fig. 7b) with streamfunction

$$\overline{\psi} = -\frac{1}{\rho\beta_0 D}\mathrm{curl}(\boldsymbol{\tau})(W - x)(1 - e^{-x/\delta_S}), \quad 0 \le x \le W, \quad (15)$$

where ρ is the density, β_0 is the planetary PV gradient, D is the water depth, $\boldsymbol{\tau}$ is the wind stress, W is the domain width, and δ_S is the western boundary layer thickness:

$$\mathrm{curl}(\boldsymbol{\tau}) = -\frac{0.35\pi}{L}\sin\left(\frac{2\pi y}{L}\right), \quad 0 \le y \le L \quad (16)$$

(Fig. 7a), analogous to the observed wind stress curl in the North Pacific (Risien and Chelton 2008). The quantity L in Eq. (16) denotes the domain length.

The value $\mathcal{F}(x, y, t)$ is modeled as a first-order autoregressive Markov process in time $n\Delta t$:

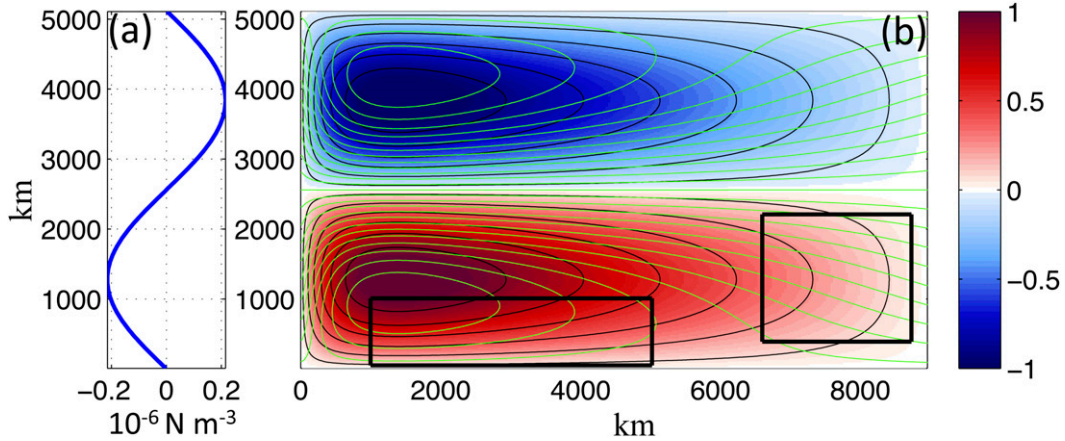$$\mathcal{F}_n = R\mathcal{F}_{n-1} + \sqrt{1 - R^2}A_n \quad (17)$$

FIG. 7. The (a) wind stress curl generates the (b) streamfunction $\overline{\psi}$ (color and black contours, $10^5 \, \text{m}^2 \, \text{s}^{-1}$) of the large-scale gyre flow. To compute $\overline{\psi}$ from Eq. (15), we use these parameters: $\rho = 1025 \, \text{kg} \, \text{m}^{-3}$, $\beta_0 = 2 \times 10^{-11} \, \text{s}^{-1} \, \text{m}^{-1}$, $D = 700 \, \text{m}$, $L = 5120 \, \text{km}$, $W = 8960 \, \text{km}$, and $\delta_S = 500 \, \text{km}$. Green contours are those of the gyre-scale potential vorticity Q. Black boxes denote the central and east regions, corresponding to the CNP and ENP regions from the ECCO2 state estimate.

(e.g., Maltrud and Vallis 1991). The term $A_n(x, y)$ is a random forcing at time $n\Delta t$ with a narrowband wavenumber spectrum:

$$A_n = \frac{\tilde{A} F^{-1}[e^{-0.01(|\mathbf{K}|^2 - K_F^2)^2 + i\theta_n(k,l)}]}{\max\{F^{-1}[e^{-0.01(|\mathbf{K}|^2 - K_F^2)^2 + i\theta_n(k,l)}]\}}, \quad (18)$$

where $\tilde{A}$ is the forcing amplitude, F^{-1} is the inverse Fourier transform operator, the wavenumber vector $\mathbf{K} = k\mathbf{i} + l\mathbf{j}$, $K_F = 0.09 \, \text{cycle grid}^{-1}$, and $\theta_n(k, l)$ are random numbers uniformly distributed between 0 and 2π. The variable R is a memory coefficient depending on both Δt and the forcing decorrelation time; the forcing is white noise if $R = 0$, and it is steady if $R = 1$ (e.g., Williams 1978; Maltrud and Vallis 1991). Here, $R = 0.7$, corresponding to a decorrelation time scale of $3\Delta t$, much shorter than the striation time scale $(2\pi\Omega_S^{-1})$, but comparable to the decorrelation time scale of observed winds (Schlax et al. 2001; Gille 2005; Monahan 2012).

Linear theories are useful in understanding many ocean aspects, such as time-mean circulation, length scale, generation, and phase speeds of eddies (e.g., Frankignoul and Müller 1979; Müller and Frankignoul 1981; Chelton et al. 2007; Tulloch et al. 2011; Wunsch 2011). Thus, we consider first Exp1, which is quasi linear with small-amplitude external forcing $(\tilde{A} = 2.7 \times 10^{-12} \, \text{s}^{-2})$. Here, the nonlinear index, defined as

$$\frac{\widetilde{|J(\psi, q)|}}{\max\left[\widetilde{|J(-Uy + Vx, q)|}, \widetilde{|J(\psi, Q)|}, \widetilde{|-rq|}\right]}, \quad (19)$$

with $\frown$ denoting the domain and time average, is only 0.1. In contrast, Exp2 is strongly forced $(\tilde{A} = 4.3 \times 10^{-11} \, \text{s}^{-2})$

and represents the nonlinear regime, as the index reaches 0.7. In both cases, the 150-yr output from a statistically equilibrated state is used. The forcing is spatially narrowband; thus, large values in the wavenumber spectrum of ψ at some frequencies are not clustered, and large areas inside the optimum ellipse correspond to small spectrum values. Thus, the method to obtain Ω_S in section 3 is not proper here. We chose Ω_S to be 1/5000 cycle day^{-1}, but the results are not sensitive to the choice. The spectral approach presented in sections 4c and 4d was developed by Chen (2013). A similar approach was later employed by Berloff and Kamenkovich (2013a,b).

c. Exp1 and linear theory

Figure 8 shows representative snapshots of external forcing, eddies, and striations in the linear experiment. The spatial scale of eddies is roughly the same as that of the external forcing. Next, we focus on the central and east regions, which are indicated by the black boxes in Fig. 8 and correspond to the CNP and ENP regions. To reveal the basic physics about the effect of mean flow on the striation direction, we further assume that U and V are constant in the central and east regions. Taking the Fourier transform of Eq. (14) with the nonlinear term $J(\psi, q)$ omitted, we obtain

$$S_\psi(k, l, \omega) = \langle |\hat{\psi}(k, l, \omega)|^2 \rangle$$
$$= \frac{\langle |\hat{\mathcal{F}}(k, l, \omega)|^2 \rangle}{(k^2 + l^2 + F_1)^2 [(\omega - \Omega_{\text{Rossby}})^2 + r^2]}, \quad (20)$$

with

$$\Omega_{\text{Rossby}} = Uk + Vl - \frac{(\beta + F_1 U)k + VF_1 l}{k^2 + l^2 + F_1}, \quad (21)$$
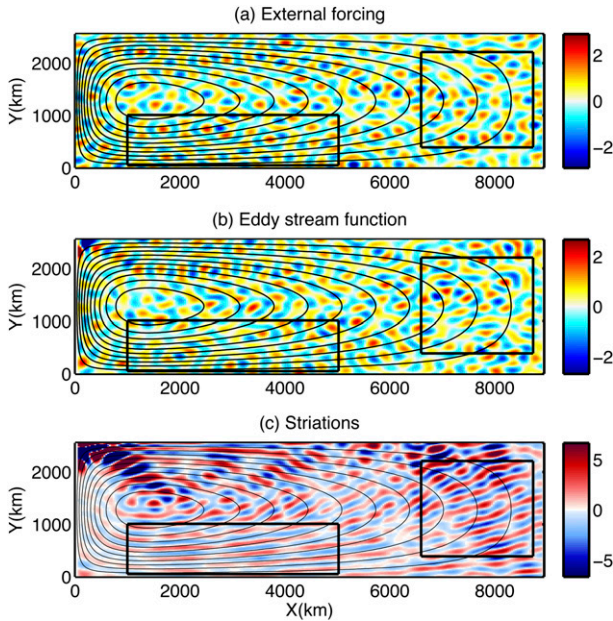
FIG. 8. Snapshots of the (a) external forcing $\mathcal{F}$ ($10^{-12}\,\mathrm{s}^{-2}$), the (b) eddy streamfunction ψ ($10^3\,\mathrm{m}^2\,\mathrm{s}^{-1}$), and the (c) part of zonal eddy velocity with frequencies lower than Ω_S ($10^{-3}\,\mathrm{m}\,\mathrm{s}^{-1}$) in the subtropical gyre in Exp1. Black boxes denote the central and east regions. Black contours are those of $\overline{\psi}$.

denoting the Doppler-shifted frequency of Rossby waves. In the inviscid or small friction case, as long as the forcing spectrum is smooth around Ω_{Rossby}, $S_\psi(k, l, \omega)$ is a maximum at $\omega = \Omega_{\mathrm{Rossby}}$. Eddies here can thus be viewed as a set of linear Rossby waves. Therefore, striations, which are bands in low-frequency motions as defined in section 3a, can be viewed as quasi-stationary (frequency $\omega \to 0$) linear Rossby waves.

Considering that bands are conspicuous and thus dominate in the low-frequency eddy field (Fig. 8), the wavenumber spectrum of striations is approximately $S_\psi(k, l, 0)$. We know from Eq. (20) that, ignoring viscosity, $S_\psi(k, l, 0)$ has large amplitudes both on the forcing circle, where $|\hat{\mathcal{F}}(k, l, 0)|$ is large, and on the zero Rossby wave frequency curve, where $\Omega_{\mathrm{Rossby}} = 0$ in wavenumber space. This inference is confirmed by the numerical analysis, shown in Figs. 9a and 9b.

The striation directions in the east and central regions are qualitatively similar to those in the ENP and CNP regions (Fig. 8). Striations occur over a range of wavenumbers and with direction roughly perpendicular to the dominant wavenumber, $\mathbf{K}_S = k_S\mathbf{i} + l_S\mathbf{j}$. This vector $\mathbf{K}_S$ occurs at the maximum value in the striation wavenumber spectrum $S_\psi(k, l, 0)$.

The maximum $S_\psi(k, l, 0)$ and thus $\mathbf{K}_S$ occur at the intersection point between the forcing circle and zero Rossby wave frequency curve, as the numerator (denominator)

of $S_\psi(k, l, 0)$ reaches the maximum (minimum) there. In the east region, the zero Rossby wave frequency curve deviates from $k = 0$, as $V \neq 0$; thus, $k_S \neq 0$ and striations are nonzonal (Fig. 9a). In the central region, the zero Rossby wave frequency curve is close to $k = 0$, as $V \approx 0$, and thus the bands are quasi zonal (Fig. 9b). To summarize, the gyre flow (U, V) influences $\mathbf{K}_S$ and thus the striation direction primarily through its effects on the zero Rossby wave frequency curve.

d. Exp2 and eddy propagation mechanism

Compared to Exp1, the spatial scale of eddies in Exp2 is larger (Figs. 10a, 8b) because of the inverse energy cascade (Okuno and Masuda 2003). Striations also exist in Exp2, but are wider than in Exp1 (Figs. 10b, 8c). Okuno and Masuda (2003) found that the formation of Rhines jets is suppressed in the nonlinear 1.5-layer system when the deformation radius R_d is smaller than $\sqrt{u_{\mathrm{eddy}}/|\nabla Q|}$, where u_{eddy} denotes the eddy velocity magnitude. This holds true in 90% of the spatial domain in Exp2, including the east and central regions.

Consistently, striations here differ in the following aspect from Rhines jets, which can occur in the nonlinear beta-plane barotropic system because of the arrest of the inverse cascade by the beta effect (Rhines 1975). Rhines jets align with the mean PV contours, but striations here do not. For example, the mean PV contours in the east region tilt southeastward and those from the central region tilts southwestward (green contours in Fig. 7), but striations from the east region tilt southwestward and those from the central region are roughly zonal (Fig. 10b).

1) MODEL SPECTRUM AND EDDY PROPAGATION MECHANISM

Spectra from Exp2 (Figs. 9c,d) are inconsistent with linear theory that predicts that striations should be concentrated on the forcing circle and the zero Rossby wave frequency curve (Figs. 9a,b). In Exp2, a large fraction of the striation spectra occurs inside the forcing circle because of the inverse cascade, and the large magnitude area is spread out because of eddy–eddy interaction.

As in the ECCO2 state estimate, striations here are roughly aligned with the eddy propagation direction (Figs. 2, 10b). Motivated by this phenomenon, we consider a conceptual model for propagating eddies. Assuming they propagate at a constant velocity,

$$\mathbf{C}_{\mathrm{eddy}} = C_x\mathbf{i} + C_y\mathbf{j}, \qquad (22)$$

with C_x and C_y denoting the zonal and meridional eddy propagation velocities. Assume also that the temporal
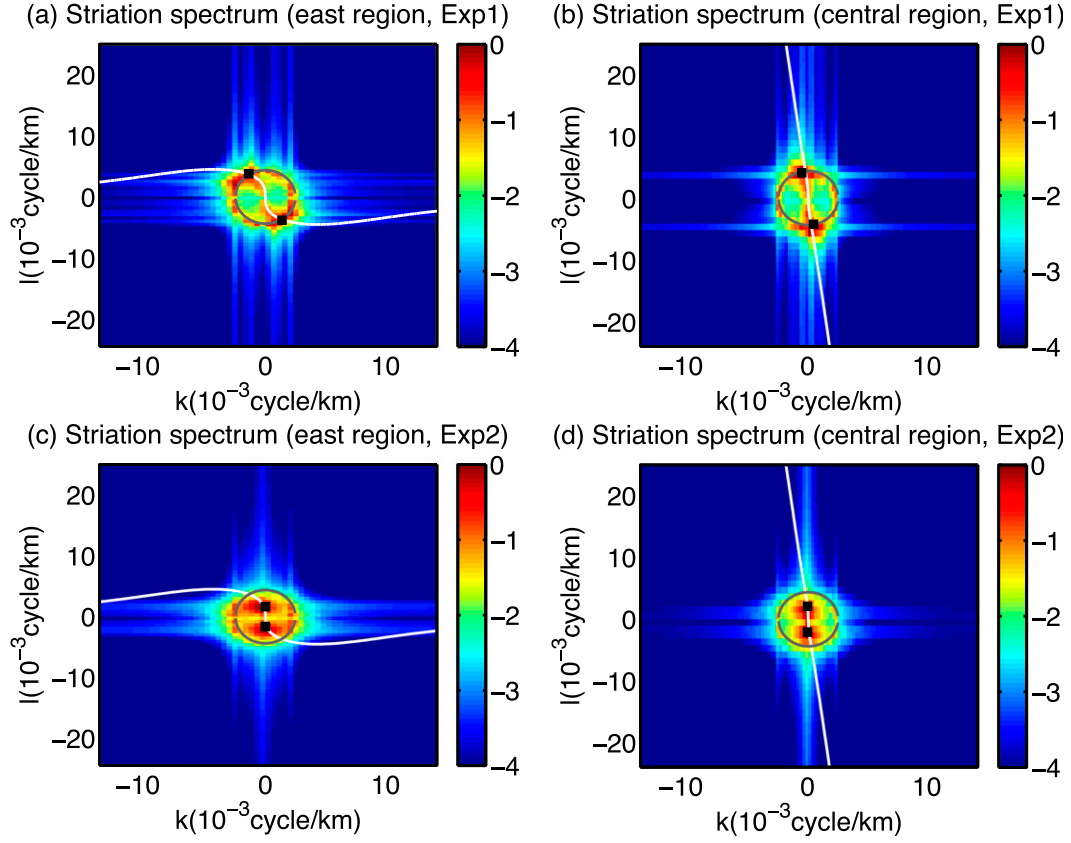
FIG. 9. The normalized wavenumber spectra of the part of ψ with frequencies lower than Ω_S in the east and central regions in (a),(b) Exp1 and (c),(d) Exp2. Black dots denote the dominant wavenumber of striations (k_S, l_S). Gray circles denote $K = K_F$, where the narrowbanded external forcing [Eqs. (17) and (18)] is concentrated on. White lines are those of $\Omega_{\text{Rossby}} = 0$. To calculate Ω_{Rossby}, the imposed gyre flow in the two regions is chosen to be the spatial average of the imposed gyre flow in the two regions. Scale of colorbars is logarithmic.

variability from processes other than eddy propagation, such as eddy–eddy interaction and external forcing variability, occurs on a slow time scale ϵt, where $\epsilon \ll 1$. Let eddy propagation occur on the fast time scale t. That is, the eddy field is quasi steady in the coordinates moving at the constant velocity $\mathbf{C}_{\text{eddy}}$. An eddy field streamfunction is,

$$\psi(x, y, t) = \phi(x - C_x t, y - C_y t, \epsilon t), \qquad (23)$$

and

$$
\begin{aligned}
\hat{\psi}(k, l, \omega) &= \int_{-\infty}^{\infty} \int_{-\infty}^{\infty} \int_{-\infty}^{\infty} \psi(x, y, t) e^{-i(kx + ly - \omega t)} \, dx \, dy \, dt \\
&= \frac{1}{\epsilon} \int_{-\infty}^{\infty} \int_{-\infty}^{\infty} \int_{-\infty}^{\infty} \phi(x', y', \tilde{T}) e^{-i[kx' + ly' - \Omega \tilde{T}]} \, dx' \, dy' \, d\tilde{T},
\end{aligned}
$$
$$(24)$$

with $x' = x - C_x t$, $y' = C_y t$, $\tilde{T} = \epsilon t$, and $\Omega = (\omega - kC_x - lC_y)/\epsilon$. The spectrum of $\psi(x, y, t)$ is

$$
\begin{aligned}
S_\psi(k, l, \omega) &= \langle |\hat{\psi}(k, l, \omega)|^2 \rangle = \left\langle \frac{1}{\epsilon^2} |\hat{\phi}(k, l, \Omega)|^2 \right\rangle \\
&= \left\langle \frac{1}{\epsilon^2} |\hat{\phi}[k, l, (\omega - kC_x - lC_y)/\epsilon]|^2 \right\rangle, \qquad (25)
\end{aligned}
$$

where

$$\hat{\phi}(k, l, \Omega) = \int_{-\infty}^{\infty} \int_{-\infty}^{\infty} \int_{-\infty}^{\infty} \phi(x, y, t) e^{-i(kx + ly - \Omega t)} \, dx \, dy \, dt. \qquad (26)$$

In the nonpropagating case (i.e., $|\mathbf{C}_{\text{eddy}}| = 0$), $S_\psi(k, l, \omega)$ is reduced to

$$S_\psi(k, l, \omega) = \left\langle \frac{1}{\epsilon^2} |\hat{\phi}(k, l, \omega/\epsilon)|^2 \right\rangle. \qquad (27)$$

Such spectra in the ocean tend to be red (e.g., Wortham 2013); assume therefore that large values in $S_\psi(k, l, \omega)$ for the nonpropagating case [Eq. (27)] occur in the low-frequency range $[-\omega_0, \omega_0]$. Note that the spectrum of propagating eddies [Eq. (25)] is just a frequency-shifted
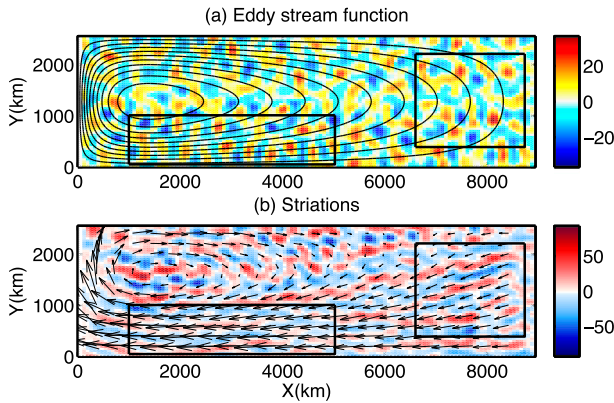
FIG. 10. Snapshots of the (a) eddy streamfunction ψ $(10^3\,\mathrm{m}^2\,\mathrm{s}^{-1})$ and the (b) part of zonal eddy velocity with frequencies lower than Ω_S $(10^{-3}\,\mathrm{m}\,\mathrm{s}^{-1})$ in Exp2. Black contours illustrate the subtropical gyre, and black boxes denote the central and east regions. Vectors denote eddy propagation velocities diagnosed using the method in appendix A. As a reference, the maximum value of these propagation velocities in the domain shown here is $0.1\,\mathrm{m}\,\mathrm{s}^{-1}$.

version of the spectrum of nonpropagating ones [Eq. (27)]. Then the largest values of propagating eddies occur in the range

$$-\omega_0 \le (\omega - kC_x - lC_y)/\epsilon \le \omega_0. \qquad (28)$$

Since $\epsilon \approx 0$, Eq. (28) is reduced to

$$\omega \approx kC_x + lC_y = \mathbf{C}_{\mathrm{eddy}} \cdot \mathbf{K} = |\mathbf{C}_{\mathrm{eddy}}|k_0. \qquad (29)$$

Large values of the frequency–wavenumber spectrum thus occur on the nondispersive line:[4] $\omega = |\mathbf{C}_{\mathrm{eddy}}|k_0$. The variables k_0 and l_0 denote the component of $\mathbf{K}$ along and across the eddy propagation direction. In analogy, we define k_{0S} and l_{0S} as the component of the dominant striation wavenumber $\mathbf{K}_S$ along and across the eddy propagation direction.

Noting that striations are bands in low-frequency motions and using Eq. (29), the striation frequency

$$\omega_S \approx \mathbf{C}_{\mathrm{eddy}} \cdot \mathbf{K}_S = |\mathbf{C}_{\mathrm{eddy}}|k_{0S} \approx 0. \qquad (30)$$

Thus,

$$\mathbf{C}_{\mathrm{eddy}} \perp \mathbf{K}_S \quad \text{and} \quad k_{0S} \approx 0. \qquad (31)$$

Assuming finite l_{0S}, low-frequency eddies are dominated by structures elongated along the eddy propagation direction.

---

[4] "Nondispersive line" here refers to the straight line, where the large values of the ω–k_0 spectrum are concentrated. Previous studies mostly focus on the nondispersive lines in the ω–k spectrum (e.g., Wortham 2013).

Therefore, striations in the idealized eddy field align with the eddy propagation direction.

Figure 11 further illustrates this interpretation. Although eddies are composed of motions with a wide range of wavenumbers, only motions with $k_0 \approx 0$ dominate at low frequencies because large values of the spectrum mostly occur on the nondispersive line [Eq. (29)]. From the kinematic and spectral perspective, striations in this idealized scenario align with the eddy propagation direction, arising as a temporal averaging effect of eddies propagating at a fixed speed. This striation interpretation will be called the "eddy propagation mechanism" to distinguish it from the "vortex propagation" one, proposed by Schlax and Chelton (2008) and summarized in section 1. These two mechanisms are compared in section 5.

2) RELEVANCE OF THE EDDY PROPAGATION MECHANISM TO EXP2

Eddies are advected by the subtropical gyre, and thus they propagate southwestward in the east region and westward in the central region (Fig. 12). As the model spectrum of the idealized propagating eddies [Eq. (25)] predicts, striations in Exp2 align with the eddy propagation direction (Fig. 10b), and the spectrum has most of its energy along the nondispersive line in the ω–k_0 space (Figs. 13a,c). As $\omega \to 0$, $k_0 \to 0$ and l_0 is finite (Figs. 13b,d), and striations are elongated in the eddy propagation direction.

The nondispersive line has also been identified in the zonal wavenumber–frequency spectrum of sea surface height from both observations and the nonlinear reduced-gravity shallow-water model (Wunsch 2009, 2010; Early et al. 2011; Wortham and Wunsch 2014). However, what sets the slope of the nondispersive line is still an open question (Ferrari and Wunsch 2010; Wortham 2013). Little is known about the quantitative effect of the meridional mean flow on the meridional eddy propagation speed, although linear theories exist for the propagation speed of vortices and planetary waves and interactions with topography and mean flows (e.g., Killworth et al. 1997; Tulloch et al. 2009).

5. Comparison between eddy propagation and vortex propagation mechanisms

a. Consistency

Schlax and Chelton (2008) proposed the vortex propagation mechanism: the temporal average of randomly seeded, westward-propagating vortices produces zonal bands. Similar to the eddy propagation mechanism from section 4d, the vortex propagation mechanism also involves the temporal averaging effect of propagating features and can be interpreted from the nondispersive line in the ω–k_0 spectra.

(a) Eddies in the snapshot
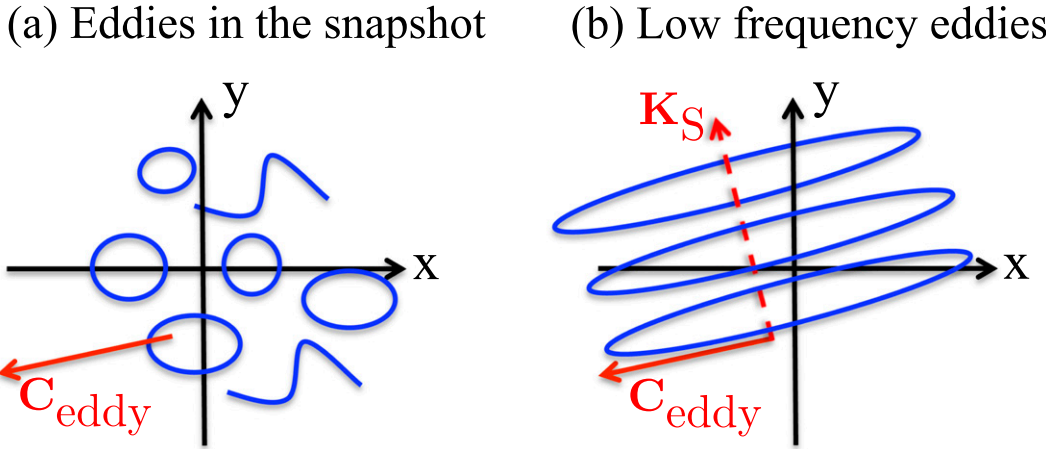

(b) Low frequency eddies

FIG. 11. This illustrates our striation interpretation based on the model spectrum [Eq. (25)]. (a) In the flow snapshot, eddies include motions over a wide range of wavenumbers and we cannot see banded structures. (b) In the low-frequency eddy field, the flow is dominated by motions with wavenumbers perpendicular to the eddy propagation direction; thus, bands along the eddy propagation direction are visible. Blue curves in (a) denote eddies, blue curves in (b) denote striations, solid red arrows denote the eddy propagation direction, and the dashed red arrow denotes direction of the dominant striation wavenumber $\mathbf{K}_S$.

1) SINGLE-VORTEX EXAMPLE

To illustrate this, we consider a highly idealized eddy field, which only contains a single Gaussian vortex, modeled as

$$\psi(x, y, t) = A e^{-(t-t_0)^2/(2T^2)} \cdot e^{-[x-x_0-(t-t_0)C_x]^2/(2L^2)}$$
$$\cdot e^{-[y-y_0-(t-t_0)C_y]^2/(2L^2)}, \tag{32}$$

with an amplitude A, size L, lifetime T, center position (x_0, y_0) at t_0, and propagating velocity $\mathbf{C}_{eddy} = C_x\mathbf{i} + C_y\mathbf{j}$. The model spectrum for this vortex is

$$S_\psi(k, l, \omega) = |\hat{\psi}(k, l, \omega)|^2$$
$$= [(2\pi)^3 L^4 T^2 A^2] e^{-(k^2+l^2)L^2-(\omega-kC_x-lC_y)^2 T^2}. \tag{33}$$

Using typical midlatitude parameters from Chelton et al. (2011), $L = 50$ km, $T = 32$ weeks, and the disturbance propagates westward with the speed 5 cm s^{-1}. The vortex lifetime T is much larger than the vortex propagation time scale $L/|\mathbf{C}_{eddy}|$; thus, the slow time ϵt is very long. Two-dimensional spectra for this midlatitude vortex from Eq. (33) show similar properties to the abstract model spectrum [Eq. (25)] as seen in Figs. 13e and 13f. Large values occur on the nondispersive line. As

$\omega \to 0$, the dominant values of $k_0 \to 0$, with l_0 remaining finite (Figs. 13e,f). The wavenumber spectrum for the zero frequency motions has the shape of a narrow ellipse with its minor axis along the k_0 direction (not shown). Thus, the low-frequency component of this propagating single vortex is elongated along the k_0 direction, as shown in Fig. 14.

2) MULTIVORTEX EXAMPLE

The example above can be extended to the case with multiple vortices, which is consistent with the scenario in Schlax and Chelton (2008). They found that the temporal average of randomly seeded westward-propagating
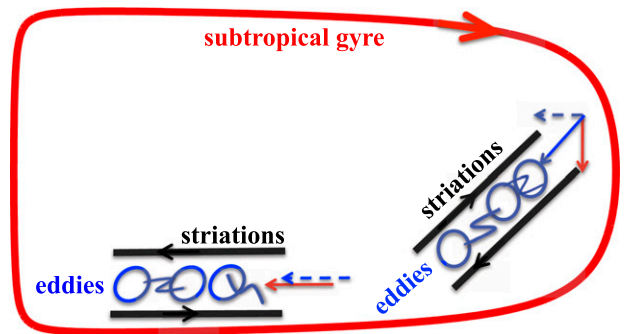

FIG. 12. Schematic diagram of the effect of the subtropical gyre (red line) on direction of striations (black lines) arising from the propagation of eddies (blue circles and curves). In the east part of the gyre, eddies propagate southwestward (solid blue arrow) instead of zonally westward (dashed blue arrow) because of the advection by the gyre (red arrow). Thus, striations there are nonzonal. In the central part of the gyre, however, directions of eddy propagation and striations are more zonal, as the gyre flow direction (red arrow) is quasi zonal.

---

[5] Here, S_ψ is the squared Fourier transform of a space–time transient and the ensemble average involved in the spectra computed from stationary random processes is not appropriate.
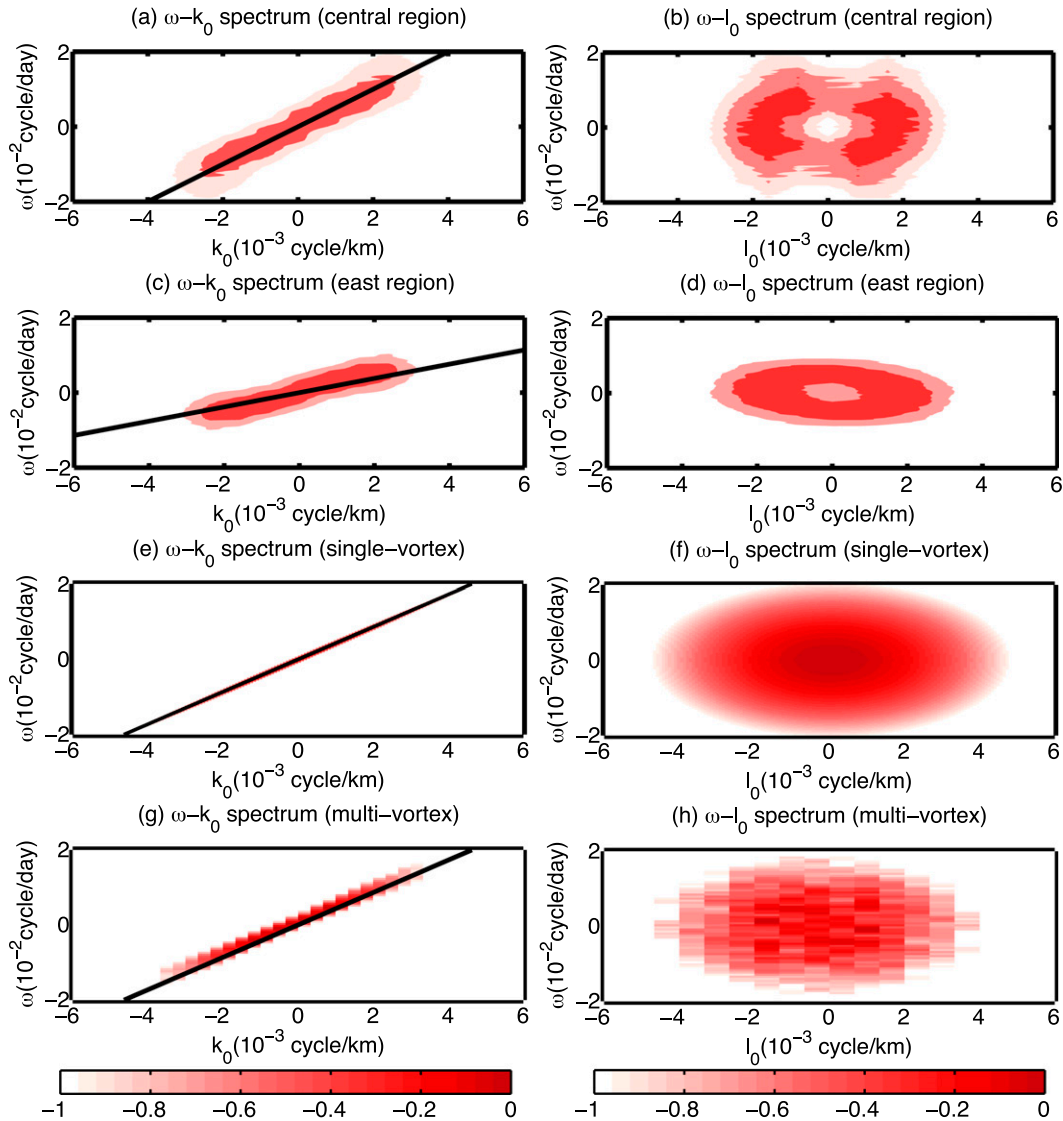
FIG. 13. Normalized ω–k_0 spectra (left) and ω–l_0 spectra (right) of ψ from Exp2 in the (a),(b) central and (c),(d) east regions, those spectra of ψ for the (e),(f) single-vortex and the (g),(h) multivortex cases. The terms k_0 and l_0, respectively, denote the wavenumbers along and perpendicular to $\mathbf{C}_{\text{eddy}}$. Black lines are $\omega = |\mathbf{C}_{\text{eddy}}|k_0$. The term $\mathbf{C}_{\text{eddy}}$ in (a)–(d) denotes the eddy propagation velocity averaged in the corresponding region in Exp2, while in (e)–(f), it refers to the eddy propagation velocity of the single vortex. In (g)–(h), it refers to the average of eddy propagation velocities of the 1000 randomly seeded vortices, described in section 5a(2). Scale of colorbars is logarithmic, and their ranges are the same for the eight panels.

vortices has zonal bands. We illustrate next that this phenomenon can also be interpreted from the nondispersive line in the ω–k_0 spectra.

Assuming the eddy streamfunction ψ is composed of a set of Gaussian vortices with amplitude A_i, size L_i, lifetime T_i, center position $(x_{0,i}, y_{0,i})$ at $t_{0,i}$, and propagating velocity $\mathbf{C}_{\text{eddy},i} = C_{x,i}\mathbf{i} + C_{y,i}\mathbf{j}$,

$$\psi(x, y, t) = \sum_{i=1}^{N} \psi_i(x, y, t), \qquad (34)$$

where

$$\psi_i(x, y, t) = H_i A_i e^{-(t-t_{0,i})^2/(2T_i^2)} e^{-[x-x_{0,i}-(t-t_{0,i})C_{x,i}]^2/(2L_i^2)}$$
$$\times e^{-[y-y_{0,i}-(t-t_{0,i})C_{y,i}]^2/(2L_i^2)}. \qquad (35)$$

Here, H_i is either 1 or -1, and thus it indicates whether the vortex is cyclone or anticyclone. The model spectrum for ψ is
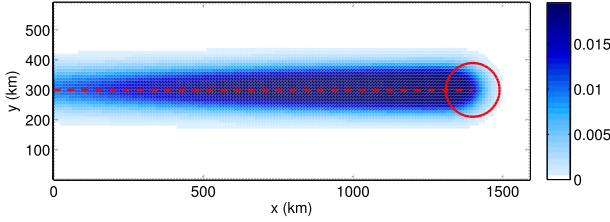
FIG. 14. The temporal average of the normalized streamfunction of the single vortex (ψ/A) over 1000 days starting from $t = t_0$. The red circle denotes the initial position of the vortex, and the red dashed line is the vortex trajectory.

$$
\begin{aligned}
S_\psi(k,l,\omega) &= \langle |\hat\psi(k,l,\omega)|^2 \rangle \\
&= \left\langle \sum_{i=1}^{N} \sum_{j=1}^{N} \hat\psi_i(k,l,\omega)\hat\psi_j{}^*(k,l,\omega) \right\rangle \\
&= \sum_{i=1}^{N} \sum_{j=1}^{N} \langle \hat\psi_i(k,l,\omega)\hat\psi_j{}^*(k,l,\omega) \rangle, \quad (36)
\end{aligned}
$$

where the asterisk denotes the complex conjugate. Assuming these random vortices are independent from each other, and $\langle \hat\psi_i \hat\psi_j{}^* \rangle$ is zero when i is not equal to j, we have

$$
S_\psi(k,l,\omega) = \left\langle \sum_{i=1}^{N} \hat\psi_i(k,l,\omega)\hat\psi_i{}^*(k,l,\omega) \right\rangle. \quad (37)
$$

A combination of Eqs. (35) and (37) leads to

$$
\begin{aligned}
&S_\psi(k,l,\omega) \\
&= \left\langle \sum_{i=1}^{N} [(2\pi)^3 L_i^4 T_i^2 A_i^2] e^{-(k^2+l^2)L_i^2 - (\omega - kC_{x,i} - lC_{y,i})^2 T_i^2} \right\rangle.
\end{aligned}
$$
$$(38)$$

Therefore, as long as these random vortices propagate roughly at the same speed, that is, the variation of $\mathbf{C}_{\mathrm{eddy},i}$ is small, the largest value of the spectra $S_\psi(k,l,\omega)$ for any given wavenumber magnitude $\sqrt{k^2 + l^2}$ occurs at

$$
\omega = kC_{x,i} + lC_{y,i} = \mathbf{C}_{\mathrm{eddy},i} \cdot \mathbf{K}. \quad (39)
$$

In other words, consistent with the single-vortex case [section 5a(1)] and Exp2 (section 4d), large values of the spectra are concentrated on the nondispersive line. Using the same argument in section 4d, we can conclude that the low-frequency component of these random vortices is elongated along the direction of $\mathbf{C}_{\mathrm{eddy},i}$, and their dominant wavenumbers are perpendicular to $\mathbf{C}_{\mathrm{eddy},i}$. Therefore, Schlax and Chelton (2008) identified the

streaks in the low-frequency component of the sea surface height field from random vortices.

To provide a specific example, we temporally and spatially randomly seeded one thousand westward-propagating vortices in a 3000 km × 1500 km domain over a 15-yr time period (Fig. 15). Properties of these vortices, including amplitudes A_i, sizes L_i, lifetimes T_i, and propagating velocities ($C_{x,i}$, $C_{y,i}$), are random numbers uniformly distributed between 80% and 120% of the typical midlatitude values, which are employed in the single-vortex example from section 5a(1). The seeding positions ($x_{0,i}$, $y_{0,i}$, $t_{0,i}$) are also uniformly distributed in the entire available spatial and temporal domain. The sign of these vortices is randomly assigned; the probability of being a cyclone or an anticyclone is equal.

A representative snapshot of ψ, composed of these random vortices, is shown in Fig. 15a. Consistent with Schlax and Chelton (2008), the low-frequency component of the zonal velocity ($-\partial/\partial y\psi$) has robust banded features (Fig. 15c). The ω–k_0 and ω–l_0 spectra from the random vortex field here are consistent with the theoretical prediction [Eq. (38)] and have similar features as those from the single-vortex case and those in Exp2 (Fig. 13).

Bands in the low-frequency zonal velocity field are narrower than those from the low-frequency ψ field (Figs. 15b,c). Because striations have low frequency and are zonally banded in this example, the spectrum of striations from the ψ field is approximately

$$
S_\psi(k,l,\omega)|_{k=0,\omega=0} = \left\langle \sum_{i=1}^{N} [(2\pi)^3 L_i^4 T_i^2 A_i^2] e^{-l^2 L_i^2} \right\rangle. \quad (40)
$$

Since $u = -\partial/\partial y\psi$, the spectrum of striations from the u field is thus

$$
S_u(k,l,\omega)|_{k=0,\omega=0} = l^2 S_\psi(k,l,\omega)|_{k=0,\omega=0}. \quad (41)
$$

Thus, the l spectrum of the low-frequency ψ is red, decreasing as l increases. However, the l spectrum of the low-frequency u field peaks at a nonzero value of l (Fig. 15d). Therefore, bands are narrower in the low-frequency zonal velocity field (Figs. 15b,c).

b. Differences

Vortex propagation and eddy propagation mechanisms are related, as both involve the temporal averaging effect of propagating features and the existence of the nondispersive line in the spectra (section 5a). On the other hand, the two mechanisms are also distinct because of the differences between "eddies" and "vortices." Vortices are roughly circular motions, trapping fluids.
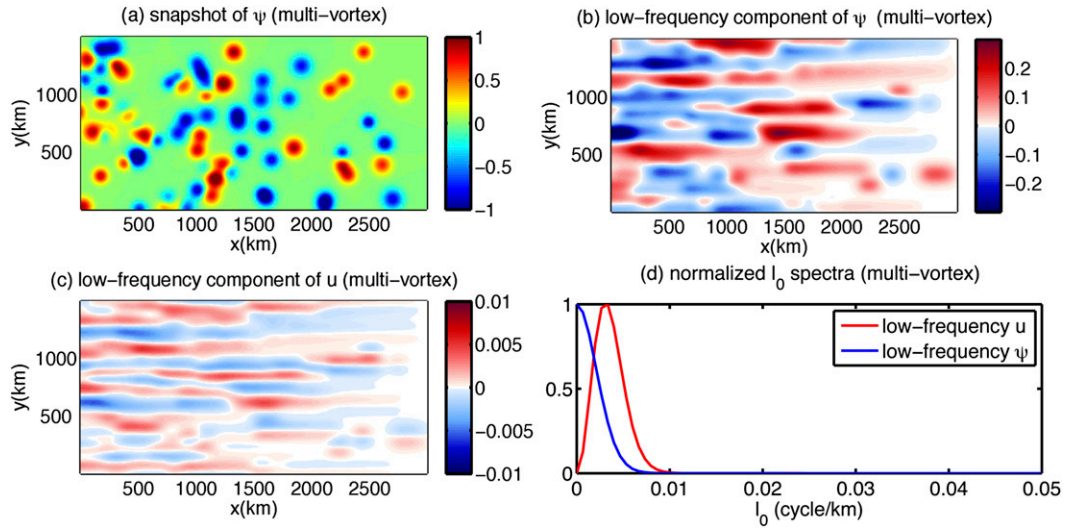
FIG. 15. This figure illustrates striations in the multivortex case. Representative snapshots of (a) ψ/A_m, (b) the low-frequency component of ψ/A_m, and (c) the low-frequency component of u/A_m (km^{-1}). (d) The normalized l_0 spectra for the low-frequency component of ψ and u. Here, u denotes the velocity along the eddy propagation direction, l_0 denotes the wavenumber across the eddy propagation direction, A_m is the mean eddy amplitude of the 1000 vortices, that is, the mean of $|A_i|$. Here, low-frequency arbitrarily refer to those lower than $\frac{1}{8}$ cycle yr^{-1}. In this case, eddies propagate zonally; thus, l_0 is just the meridional wavenumber l.

Eddies in this study, however, refer to anomalies, that is, deviations from the long-term time mean.

The eddy field includes both vortices and background motions (e.g., McWilliams 1984; Elhmaïdi et al. 1993; Polvani et al. 1994; Chelton et al. 2011). The separation of the two components is often based on the Okubo–Weiss parameter (Okubo 1970; Weiss 1991):

$$\mathcal{OW} = \underbrace{[(\partial_x u - \partial_y v)^2 + (\partial_x v + \partial_y u)^2]}_{s^2} - \underbrace{(\partial_x v - \partial_y u)^2}_{\omega^2},$$
(42)

where s^2 and ω^2 measure deformation and rotation, respectively (e.g., Isern-Fontanet et al. 2004; Chelton et al. 2007; Chaigneau et al. 2008). Vortices, in which rotation dominates, correspond to negative $\mathcal{OW}$ (e.g., Chelton et al. 2007; Buckingham and Cornillon 2013). The rest of the eddy field is defined as background motions.

Buckingham and Cornillon (2013) analyzed the altimeter data and found that both the temporal average of vortices and the temporal average of background motions have banded structures. Using the Okubo–Weiss parameter, we split ψ in Exp2 into a vortex part (ψ_V) and a background part (ψ_B) (Fig. 16a):

$$\psi(x, y, t) = \psi_V(x, y, t) + \psi_B(x, y, t),$$
(43)

where

$$\psi_V = \begin{cases} 0 & \text{if} \quad \mathcal{OW} > 0 \\ \psi & \text{if} \quad \mathcal{OW} < 0 \end{cases} \quad \text{and} \quad \psi_B = \begin{cases} \psi & \text{if} \quad \mathcal{OW} > 0 \\ 0 & \text{if} \quad \mathcal{OW} < 0. \end{cases}$$

Consistent with Buckingham and Cornillon (2013), the low-frequency parts of ψ_V and ψ_B both have banded structures (Fig. 16). Nondispersive lines exist in the ω–k_0 spectra of both ψ_V and ψ_B (not shown). Therefore, striations from both ψ_V and ψ_B arise as the temporal averaging effect of eddies propagating in the fixed direction. To conclude, the vortex propagation mechanism is essentially about how vortices contribute to the striation formation; however, the eddy propagation mechanism illustrates that the nondispersively propagating vortices and background motions both contribute to the striation formation.

6. Conclusions and discussion

In the subtropical gyre of the central and eastern North Pacific (CNP and ENP) regions, a nonnegligible percentage of zonal velocity variability is associated with banded structures. Though spectral analysis using a 1.5-layer model, we identified two interpretations of striations: quasi-stationary linear waves (linear wave mechanism) and the low-frequency component of nondispersively propagating eddies (eddy propagation mechanism). How the gyre flow affects the band directions is different in the two cases. The above striations interpretations are based on conceptual spectral models: linear waves are the motions satisfying the dispersion relation in the
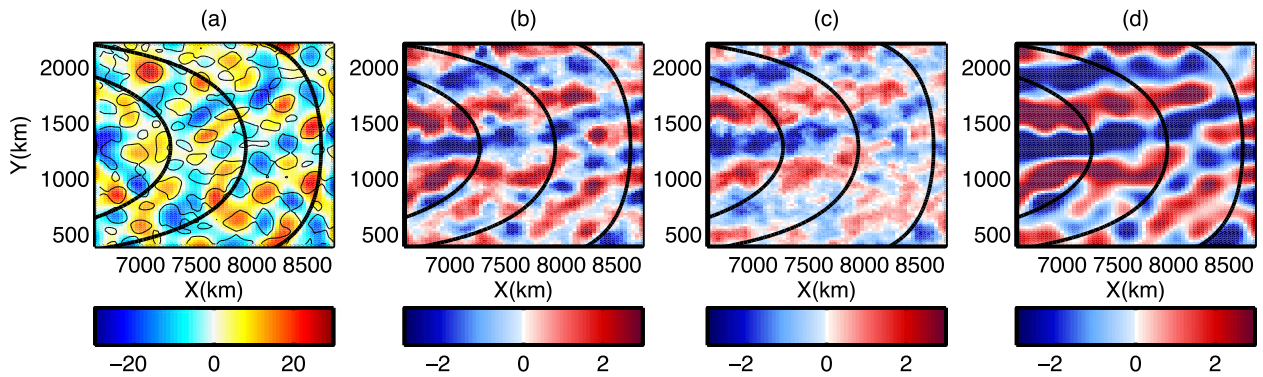
FIG. 16. Representative snapshots of (a) ψ (10^3 m^2 s^{-1}), the (b) part of ψ_V (10^3 m^2 s^{-1}), (c) ψ_B (10^3 m^2 s^{-1}), and (d) ψ (10^3 m^2 s^{-1}) with frequencies lower than Ω_S in the east region from Exp2. In (b)–(d), black lines denote the gyre flow; in (a), the thick black contours are those of the gyre flow and the thin black lines are the zero contours for the Okubo–Weiss parameter $\mathcal{OW}$.

frequency–wavenumber space and the linearized equations of motion, and nondispersively propagating eddies are the motions occurring at the nondispersive surface [Eq. (29)] in the frequency–wavenumber space.

The nonlinear eddy propagation mechanism presented in Exp2 is probably relevant to striations in the ocean interior between a few degrees off the equator and 45°. Wortham (2013) found that the ω–k spectra of sea surface height from the altimetry have nondispersive lines in these regions. The rough consistency between the eddy trajectories and the striation directions in the CNP region and the southern part of the ENP region further suggests the relevance of the eddy propagation mechanism there (Fig. 2). The wave mechanism in Exp1 might apply to some extent in the equatorial regions, as eddies there are dominated by waves (Tulloch et al. 2009). For example, the amplitude and positions of the time-mean barotropic jets are overall consistent with the linear wind-driven solutions in the equatorial South Pacific (e.g., Kessler and Gourdeau 2006; Taguchi et al. 2012). However, our theory about the impact of mean flow on the direction of wavelike striations [Eqs. (20) and (21)] is based on the assumption that the mean flow is constant; thus, it does not apply in the regions where the mean flow shear is large.

Nondispersive lines are absent in the ω–k spectra in the western boundary current and its extension regions, the subpolar gyres and the Southern Ocean (Wortham 2013), and the eddy propagation mechanism as described here would not be relevant. Other observations, however, have been interpreted as showing banded structures there (e.g., Fig. 1 in Maximenko et al. 2008). In the Gulf Stream and Kuroshio Extension regions, both westward and eastward eddy propagation are important (Wortham 2013), and some other process may be active. In the Southern Ocean, eddy propagation speed is highly inhomogeneous because of the small-scale topography

steering and jet meandering and so on (Fu 2009). Slow eddy propagation speeds in high latitudes, and the corresponding difficulty of separating fast and slow times there [i.e., ϵ from Eq. (28) is large], means that a separate analysis is required.

Section 5 compares the eddy propagation and vortex propagation mechanisms. Our multivortex case [section 5a(2)] is consistent with Schlax and Chelton (2008): the temporal average of randomly seeded westward-propagating vortices has zonal bands. Yet, we gained other insights: 1) the phenomenon that the temporal average of propagating motions has banded structures is consistent with the nondispersive line in the ω–k_0 spectra; 2) our striation definition in section 3a suggests that these bands are part of the propagating eddy field; 3) $\epsilon \approx 0$ is a prerequisite for the existence of these banded structures in the low-frequency eddy field; and 4) while the vortex propagation mechanism focus on striations from the propagation of vortices, the eddy propagation mechanism means that both propagating vortices and propagating background motions have banded structures at low frequencies. Note that eddies in this study denote deviation from the long-term time mean, which include both vortices (roughly circular motions) and the background field.

Further interpretation of the eddy propagation mechanism is left for future work. The dynamic reasons for the formation of the nondispersive line in the spectra remain unclear. Besides the Okubo–Weiss parameter, other methods to split eddies into vortices and background motions exist, such as the winding angle method and the wavelet transform method (e.g., Ari Sadarjoen and Post 2000; Ruppert-Felsot et al. 2005; Zhan et al. 2014). Descriptions and theories about the respective contribution of vortices and the background field to the nondispersive line and to striation energy remain to be done.

One eddy propagation mechanism does not include all the striations. First, altimetric observations indicate that

besides transient striations, stationary jets probably also exist (Maximenko et al. 2005, 2008). The eddy propagation mechanism captures striations in propagating eddies, which are time dependent, and thus this mechanism does not include stationary jets. Second, in the area away from the nondispersive line in the ω–k_0 space, the values of the spectra are small but nonzero, and weak eddies exist. Some of these eddies have elongated structures and are also striations, which cannot be explained by the eddy propagation mechanism.

One limitation of this study arises from the use of the 1.5-layer model. Other dynamical factors must affect striations, including topography, vertical mode coupling, and time dependence of the gyre flow. Beta plumes may also be relevant to striations in the CNP region, and radiating instabilities contribute to striation formation in the ENP region (Belmadani et al. 2013; Wang et al. 2013). No comprehensive theory exists.

More than 20% of the eddy kinetic and eddy available potential energies are associated with striations in the CNP region (section 3b). Thus, the role of striations in eddy energy budgets can be significant in at least some regions. Because they are coherent in the along striation direction, shear dispersion and thus anisotropic transports result. Chen (2013) provided diagnostic frameworks. Quantitative analysis of their role in mixing and movement/transformation of energy in the global ocean remains to be done.

APPENDIX A

Calculation of Eddy Propagation Velocity

We define $E(x, y, t)$ as an eddy variable at time t (e.g., eddy kinetic energy) in an oceanic patch with width L_x and length L_y, centered at the location (x, y). Therefore, $E(x + \delta x, y + \delta y, t + \delta t)$ represents the variable at time $t + \delta t$ in the neighboring patch centered at $(x + \delta x, y + \delta y)$. The spatial correlation between $E(x, y, t)$ and $E(x + \delta x, y + \delta y, t + \delta t)$ is defined as $\gamma(x, y, t, \delta x, \delta y, \delta t)$. For a specific location (x, y), time t, and time lag δt, if γ reaches its maximum value γ_0 when

$$x = \delta x_0, \quad y = \delta y_0, \tag{A1}$$

we assume eddies in the patch centered at (x, y) at time t propagate to the patch centered at $(x + \delta x_0, y + \delta y_0)$ at time $t + \delta t$. Note that $\delta x_0, \delta y_0$, and γ_0 are all functions of x, y, t, and δt. We can choose a range of values for δt, denoted by δt_n.

Similar to Fu (2009), our eddy propagation velocity in the patch centered at the location (x, y) is essentially the weighted average of propagation velocities over a range of time t and time lag δt_n, that is,

$$\mathbf{C}_{\text{eddy}}(x, y) = \frac{\sum_n \int \{[\delta x_0(x, y, t, \delta t_n)/\delta t_n \mathbf{i} + \delta y_0(x, y, t, \delta t_n)/\delta t_n \mathbf{j}]\gamma_0(x, y, t, \delta t_n)\} \, dt}{\sum_n \int \gamma_0(x, y, t, \delta t_n) \, dt}. \tag{A2}$$

Weights are correlation coefficients γ_0. In this study, we choose eddy kinetic energy as $E(x, y, t)$. In the ECCO2 model diagnosis, L_x and L_y are chosen to be 3°, the variation range of δ_x and δ_y are from $-2°$ to 2°, and δt_n are from 9 to 69 days at the 6-day interval. In the 1.5-layer model diagnosis, both L_x and L_y are 9 model grids, both δ_x and δ_y range from -5 to 5 model grids, and δt_n have two values (5 and 10 days).

APPENDIX B

An Alternative Derivation of the Idealized Model

Pedlosky (1984) used a multiple-scale expansion method and developed a stratified quasigeostrophic model for mesoscale motion; one permitting a slow variation of the background stratification from the gyre-scale flow. With the same scaling, one can obtain the 1.5-layer model:

$$\left[\frac{\partial}{\partial t} + (\mathbf{U} + \mathbf{u}') \cdot \nabla_x\right]\left(\zeta' - f\frac{h'}{H}\right) + \mathbf{u}' \cdot \left(H\nabla_X\frac{f}{H}\right) = \mathcal{F}, \tag{B1}$$

where $\mathbf{U}, \mathbf{u}'$ are the gyre-scale and mesoscale velocities, H, h' are the corresponding layer thickness, f is the Coriolis parameter, ζ' is the mesoscale relative vorticity, $\mathcal{F}$ is the mesoscale forcing, and $\mathbf{V}$ is the horizontal gradient operator. Gyre-scale fields vary on long scales $(\mathbf{X}, T)$

and mesoscale fields vary on short ones $(\mathbf{x}, t)$. To solve Eq. (B1) numerically, we express it in terms of eddy streamfunction following Theiss (2004), add the friction term, and then get Eq. (14). Next, we illustrate how to derive Eq. (B1).

We start our derivation from the shallow-water equations:

$$\left(\frac{\partial}{\partial t} + \mathbf{u} \cdot \nabla\right) u - f\upsilon = -g'\frac{\partial}{\partial x}h, \qquad (B2)$$

$$\left(\frac{\partial}{\partial t} + \mathbf{u} \cdot \nabla\right) \upsilon + fu = -g'\frac{\partial}{\partial y}h, \quad \text{and} \qquad (B3)$$

$$\frac{\partial h}{\partial t} + \frac{\partial}{\partial x}(hu) + \frac{\partial}{\partial y}(h\upsilon) = -w_e, \qquad (B4)$$

where g' is the reduced gravity, h is the layer thickness, and w_e is the Ekman pumping velocity. The variables $\mathbf{u}$, u, and υ are, respectively, the velocity vector, zonal, and meridional velocities.[6] Friction is ignored in the momentum equations for simplicity. Instead of putting wind stress in the momentum equation, we include the wind forcing by adding an Ekman pumping term in the mass conservation equation, as that in section 4.1 of Huang (2010). Cross-differentiating Eqs. (B2) and (B3) and using Eq. (B4), we obtain the PV equation

$$\left(\frac{\partial}{\partial t} + \mathbf{u} \cdot \nabla\right)\frac{f + \zeta}{h} = \frac{(f + \zeta)w_e}{h^2}, \qquad (B5)$$

where ζ denotes the relative vorticity $\partial\upsilon/\partial x - \partial u/\partial y$.

As in Pedlosky (1984), we separate the variables into two parts:

$$\mathbf{u}(\mathbf{x}, t) = U_0[\mathbf{U}(\mathbf{X}, T) + \mathbf{u}'(\mathbf{x}', t', \mathbf{X}, T)], \quad \text{and} \qquad (B6)$$

$$h(\mathbf{x}, t) = H_0[H(\mathbf{X}, T) + \delta h'(\mathbf{x}', t', \mathbf{X}, T)]. \qquad (B7)$$

The terms $\mathbf{U}$ and H are the gyre-scale part, $\mathbf{u}'$ and $\delta h'$ are the mesoscale part, $(\mathbf{X}, T)$ are the coordinate for the gyre-scale variation, and $(\mathbf{x}', t')$ are the coordinate for the mesoscale variation. The key assumption in Pedlosky (1984) is that the gyre scale is much larger and slower than the mesoscale, that is,

$$\mathbf{X} = \mathbf{x}/L, \quad \mathbf{x}' = \mathbf{x}/l, \quad t' = \sigma t, \quad T = t'l/L, \quad \delta = l/L \ll 1, \qquad (B8)$$

where δ is the scale ratio, and σ is the advection time on mesoscale (i.e., U_0/l). Also we scale the Coriolis

---

---

parameter: $f = f_0 f'(Y)$. Now we can write the spatial and temporal derivatives in the gyre-scale and mesoscale coordinates:

$$\frac{\partial}{\partial x} = \frac{1}{l}\left(\delta\frac{\partial}{\partial X} + \frac{\partial}{\partial x'}\right), \quad \frac{\partial}{\partial y} = \frac{1}{l}\left(\delta\frac{\partial}{\partial Y} + \frac{\partial}{\partial y'}\right), \quad \text{and}$$

$$\frac{\partial}{\partial t} = \frac{U_0}{l}\left(\delta\frac{\partial}{\partial T} + \frac{\partial}{\partial t'}\right). \qquad (B9)$$

Using Eqs. (B6)–(B9), the momentum equations [Eqs. (B2) and (B3)] can be nondimensionalized as

$$\epsilon D_x(\mathbf{U} + \mathbf{u}') + \epsilon\delta D_X(\mathbf{U} + \mathbf{u}') + f\hat{k} \times (\mathbf{U} + \mathbf{u}')$$
$$= -\nabla_X(H + \delta h') - \nabla_x h', \qquad (B10)$$

where $\epsilon = U_0/f_0 l$ and $g'H_0 = f_0 U_0 L$. The operators D_X and D_x denote

$$D_X = \frac{\partial}{\partial T} + (\mathbf{U} + \mathbf{u}') \cdot \nabla_X, \quad D_x = \frac{\partial}{\partial t} + (\mathbf{U} + \mathbf{u}') \cdot \nabla_x.$$

The primes in $\mathbf{x}'$, t', and f' are dropped in Eq. (B10) for simplicity and this simplification is also used for the rest of this appendix. The nondimensional PV is

$$q = \frac{f + \epsilon\zeta' + \epsilon\delta(V_X - U_Y + \upsilon'_X - u'_Y)}{H + \delta h'}$$
$$= Q(\mathbf{X}, t) + \delta\tilde{q}(\mathbf{x}, t, \mathbf{X}, T), \qquad (B11)$$

with

$$\zeta' = \frac{\partial\upsilon'}{\partial x} - \frac{\partial u'}{\partial y}, \quad Q = \frac{f}{H},$$

$$\tilde{q} = \frac{1}{H + \delta h'}\left[\frac{\epsilon}{\delta}\zeta' - \frac{f}{H}h' + \epsilon(V_X - U_Y + \upsilon'_X - u'_Y)\right]. \qquad (B12)$$

We can then get the nondimensional PV equation from Eqs. (B5) and (B11):

$$D_X Q + D_x\tilde{q} + \delta D_X\tilde{q} = F_X + F'_x, \qquad (B13)$$

where F_X is the gyre-scale forcing, and F'_x is the mesoscale forcing. Also,

$$F_X + F'_x \approx \frac{Lw_{e0}}{H_0 U}[W_e(\mathbf{X}, T) + w'_e(\mathbf{x}, t, \mathbf{X}, T)]\frac{f}{H^2}, \qquad (B14)$$

where $w_{e0}[W_e(\mathbf{X}, T) + w'_e(\mathbf{x}, t, \mathbf{X}, T)] = w_e$.

Assuming $\delta \sim \epsilon \ll 1$, the lowest-order momentum and PV equations are

$$f\hat{\mathbf{k}} \times \mathbf{U} + f\hat{\mathbf{k}} \times \mathbf{u}' = -\nabla_X H - \nabla_x h', \quad \text{and} \qquad (B15)$$

$$\left[\frac{\partial}{\partial T} + \mathbf{U} \cdot \boldsymbol{\nabla}_X\right]Q + \mathbf{u}' \cdot \boldsymbol{\nabla}_X Q + \left[\frac{\partial}{\partial t} + (\mathbf{U} + \mathbf{u}') \cdot \boldsymbol{\nabla}_x\right]q'$$
$$= F_X + F_x',$$

(B16)

where $\hat{\mathbf{k}}$ is the unit vector in the vertical direction, and

$$q' = \frac{1}{H}\left(\frac{\epsilon}{\delta}\zeta' - \frac{f}{H}h'\right).$$

Equations (B15) and (B16) can be separated into the part independent of $\mathbf{x}$ and the rest. Setting each part to zero, we can get the leading order balances for gyre-scale motions $\mathbf{U}$ and the leading order balances for mesoscale motions $\mathbf{u}'$, as listed below:

$$f\hat{\mathbf{k}} \times \mathbf{U} = -\boldsymbol{\nabla}_X H,$$

(B17)

$$\left[\frac{\partial}{\partial T} + \mathbf{U} \cdot \boldsymbol{\nabla}_X\right]Q = F_X,$$

(B18)

$$f\hat{\mathbf{k}} \times \mathbf{u}' = -\boldsymbol{\nabla}_x h', \quad \text{and}$$

(B19)

$$\left[\frac{\partial}{\partial t} + (\mathbf{U} + \mathbf{u}') \cdot \boldsymbol{\nabla}_x\right]q' + \mathbf{u}' \cdot \boldsymbol{\nabla}_X Q = F_x'.$$

(B20)

The dimensional counterpart of Eq. (B20) is Eq. (B1).

REFERENCES

Afanasyev, Y. D., S. O. Leary, P. B. Rhines, and E. G. Lindahl, 2012: On the origin of jets in the ocean. *Geophys. Astrophys. Fluid Dyn.,* **106,** 113–137, doi:10.1080/03091929.2011.562896.

Ari Sadarjoen, I., and F. H. Post, 2000: Detection, quantification, and tracking of vortices using streamline geometry. *Comput. Graphics,* **24,** 333–341, doi:10.1016/S0097-8493(00)00029-7.

Baldwin, M., P. B. Rhines, H.-P. Huang, and M. E. McIntyre, 2007: The jet-stream conundrum. *Science,* **315,** 467–468, doi:10.1126/science.1131375.

Belmadani, A., N. A. Maximenko, J. P. McCreary, R. Furue, O. V. Melnichenko, N. Schneider, and E. D. Lorenzo, 2013: Linear wind-forced beta-plumes with application to the Hawaiian Lee Countercurrent. *J. Phys. Oceanogr.,* **43,** 2071–2094, doi:10.1175/JPO-D-12-0194.1.

Berloff, P., 2005: On rectification of randomly forced flows. *J. Mar. Res.,* **63,** 497–527, doi:10.1357/0022240054307894.

——, and I. Kamenkovich, 2013a: On spectral analysis of mesoscale eddies. Part I: Linear analysis. *J. Phys. Oceanogr.,* **43,** 2505–2527, doi:10.1175/JPO-D-12-0232.1.

——, and ——, 2013b: On spectral analysis of mesoscale eddies. Part II: Nonlinear analysis. *J. Phys. Oceanogr.,* **43,** 2528–2544, doi:10.1175/JPO-D-12-0233.1.

——, S. Karabasov, J. T. Farrar, and I. Kamenkovich, 2011: On latency of multiple zonal jets in the oceans. *J. Fluid Mech.,* **686,** 534–567, doi:10.1017/jfm.2011.345.

Boland, E. J. D., A. F. Thompson, E. Shuckburgh, and P. H. Haynes, 2012: The formation of nonzonal jets over sloped topography. *J. Phys. Oceanogr.,* **42,** 1635–1651, doi:10.1175/JPO-D-11-0152.1.

Buckingham, C. E., and P. C. Cornillon, 2013: The contribution of eddies to striations in absolute dynamic topography. *J. Geophys. Res.,* **118,** 448–461, doi:10.1029/2012JC008231.

Centurioni, L. R., J. C. Ohlmann, and P. P. Niiler, 2008: Permanent meanders in the California Current system. *J. Phys. Oceanogr.,* **38,** 1690–1710, doi:10.1175/2008JPO3746.1.

Chaigneau, A., A. Gizolme, and C. Grados, 2008: Mesoscale eddies off Peru in altimeter records: Identification algorithms and eddy spatio-temporal patterns. *Prog. Oceanogr.,* **79,** 106–119, doi:10.1016/j.pocean.2008.10.013.

Chelton, D. B., M. G. Schlax, R. M. Samelson, and R. A. de Szoeke, 2007: Global observations of large oceanic eddies. *Geophys. Res. Lett.,* **34,** L15606, doi:10.1029/2007GL030812.

——, ——, and ——, 2011: Global observations of nonlinear mesoscale eddies. *Prog. Oceanogr.,* **91,** 167–216, doi:10.1016/j.pocean.2011.01.002.

Chen, R., 2013: Energy pathways and structures of oceanic eddies from the ECCO2 state estimate and simplified models. Ph.D. thesis, Massachusetts Institute of Technology and Woods Hole Oceanographic Institution, 206 pp.

Cox, M., 1987: An eddy-resolving numerical model of the ventilated thermocline: Time dependence. *J. Phys. Oceanogr.,* **17,** 1044–1056, doi:10.1175/1520-0485(1987)017<1044: AERNMO>2.0.CO;2.

Cushman-Roisin, B., B. Tang, and E. P. Chassignet, 1990: Westward motion of mesoscale eddies. *J. Phys. Oceanogr.,* **20,** 758–768, doi:10.1175/1520-0485(1990)020<0758:WMOME>2.0.CO;2.

Dibarboure, G., O. Lauret, F. Mertz, V. Rosmorduc, and C. Maheu, 2009: SSALTO/DUACS user handbook: (M)SLA and (M)ADT near-real time and delayed time products. AVISO Altimetry Rep. CLS-DOS-NT-06.034, 51 pp.

Early, J. J., R. M. Samelson, and D. B. Chelton, 2011: The evolution and propagation of quasigeostrophic ocean eddies. *J. Phys. Oceanogr.,* **41,** 1535–1555, doi:10.1175/2011JPO4601.1.

Elhmaïdi, D., A. Provenzale, and A. Babiano, 1993: Elementary topology of two-dimensional turbulence from a Lagrangian viewpoint and single-particle dispersion. *J. Fluid Mech.,* **257,** 533–558, doi:10.1017/S0022112093003192.

Ferrari, R., and C. Wunsch, 2009: Ocean circulation kinetic energy—Reservoirs, sources and sinks. *Annu. Rev. Fluid Mech.,* **41,** 253–282, doi:10.1146/annurev.fluid.40.111406.102139.

——, and ——, 2010: The distribution of eddy kinetic and potential energies in the global ocean. *Tellus,* **62A,** 92–108, doi:10.1111/j.1600-0870.2009.00432.x.

Frankignoul, C., and P. Müller, 1979: Quasi-geostrophic response of an infinite β-plane ocean to stochastic forcing by the atmosphere. *J. Phys. Oceanogr.,* **9,** 104–127, doi:10.1175/1520-0485(1979)009<0104:QGROAI>2.0.CO;2.

Fu, L.-L., 2009: Pattern and velocity of propagation of the global ocean eddy variability. *J. Geophys. Res.,* **114,** C11017, doi:10.1029/2009JC005349.

Galperin, B., H. Nakano, H. P. Huang, and S. Sukoriansky, 2004: The ubiquitous zonal jets in the atmospheres of giant planets and Earth's oceans. *Geophys. Res. Lett.,* **31,** L13303, doi:10.1029/2004GL019691.

Gille, S. T., 2005: Statistical characterization of zonal and meridional ocean wind stress. *J. Atmos. Oceanic Technol.,* **22,** 1353–1372, doi:10.1175/JTECH1789.1.

Hristova, H. G., J. Pedlosky, and M. A. Spall, 2008: Radiating instability of a meridional boundary current. *J. Phys. Oceanogr.,* **38,** 2294–2307, doi:10.1175/2008JPO3853.1.

Huang, R. X., 2010: *Ocean Circulation: Wind-Driven and Thermohaline Processes.* Cambridge University Press, 806 pp.

Isern-Fontanet, J., J. Font, E. García-Ladona, M. Emelianov, C. Millot, and I. Taupier-Letage, 2004: Spatial structure of anticyclonic eddies in the Algerian basin (Mediterranean Sea) analyzed using the Okubo–Weiss parameter. *Deep-Sea Res. II,* **51,** 3009–3028, doi:10.1016/j.dsr2.2004.09.013.

Jacob, J. P., E. P. Chassignet, and W. K. Dewar, 2002: Influence of topography on the propagation of isolated eddies. *J. Phys. Oceanogr.,* **32,** 2848–2869, doi:10.1175/1520-0485(2002)032<2848: IOTOTP>2.0.CO;2.

Kamenkovich, I., P. Berloff, and J. Pedlosky, 2009: Anisotropic material transport by eddies and eddy-driven currents in a model of the North Atlantic. *J. Phys. Oceanogr.,* **39,** 3162–3175, doi:10.1175/2009JPO4239.1.

Kessler, W. S., and L. Gourdeau, 2006: Wind-driven zonal jets in the South Pacific Ocean. *Geophys. Res. Lett.,* **33,** L03608, doi:10.1029/2005GL025084.

Killworth, P. D., D. B. Chelton, and R. A. de Szoeke, 1997: The speed of observed and theoretical long extratropical planetary waves. *J. Phys. Oceanogr.,* **27,** 1946–1966, doi:10.1175/ 1520-0485(1997)027<1946:TSOOAT>2.0.CO;2.

Klocker, A., R. Ferrari, and J. H. LaCasce, 2012: Estimating suppression of eddy mixing by mean flows. *J. Phys. Oceanogr.,* **42,** 1566–1576, doi:10.1175/JPO-D-11-0205.1.

Maltrud, M., and G. K. Vallis, 1991: Energy spectra and coherent structures in forced two-dimensional and geostrophic turbulence. *J. Fluid Mech.,* **228,** 321–342.

Maximenko, N. A., B. Bang, and H. Sasaki, 2005: Observational evidence of alternating zonal jets in the world ocean. *Geophys. Res. Lett.,* **32,** L12607, doi:10.1029/2005GL022728.

——, O. V. Melnichenko, P. P. Niiler, and H. Sasaki, 2008: Stationary mesoscale jet-like features in the ocean. *Geophys. Res. Lett.,* **35,** L08603, doi:10.1029/2008GL033267.

McWilliams, J. C., 1984: The emergence of isolated coherent vortices in turbulent flow. *J. Fluid Mech.,* **146,** 21–43, doi:10.1017/ S0022112084001750.

——, and G. R. Flierl, 1979: On the evolution of isolated, nonlinear vortices. *J. Phys. Oceanogr.,* **9,** 1155–1182, doi:10.1175/ 1520-0485(1979)009<1155:OTEOIN>2.0.CO;2.

Menemenlis, D., J.-M. Campin, P. Heimbach, C. Hill, T. Lee, A. Nguyen, M. Schodlock, and H. Zhang, 2008: ECCO2: High resolution global ocean and sea ice data synthesis. *Mercator Ocean Quarterly Newsletter,* No. 31, Mercator Ocean, Ramonville Saint-Agne, France, 13–21.

Monahan, A. H., 2012: The temporal autocorrelation structure of sea surface winds. *J. Climate,* **25,** 6684–6700, doi:10.1175/ JCLI-D-11-00698.1.

Müller, P., and C. Frankignoul, 1981: Direct atmospheric forcing of geostrophic eddies. *J. Phys. Oceanogr.,* **11,** 287–308, doi:10.1175/ 1520-0485(1981)011<0287:DAFOGE>2.0.CO;2.

Nakano, H., and H. Hasumi, 2005: A series of zonal jets embedded in the broad zonal flows in the Pacific obtained in eddy-permitting ocean general circulation models. *J. Phys. Oceanogr.,* **35,** 474–488, doi:10.1175/JPO2698.1.

Okubo, A., 1970: Horizontal dispersion of floatable particles in the vicinity of velocity singularities such as convergences. *Deep-Sea Res. Oceanogr. Abstr.,* **17,** 445–454, doi:10.1016/ 0011-7471(70)90059-8.

Okuno, A., and A. Masuda, 2003: Effect of horizontal divergence on the geostrophic turbulence on a beta-plane: Suppression of the Rhines effect. *Phys. Fluids,* **15,** 56–65, doi:10.1063/1.1524188.

Oort, A., S. Ascher, S. Levitus, and J. Peixóto, 1989: New estimates of the available potential energy in the World Ocean. *J. Geophys. Res.,* **94,** 3187–3200, doi:10.1029/JC094iC03p03187.

O'Reilly, C. H., A. Czaja, and J. H. LaCasce, 2012: The emergence of zonal ocean jets under large-scale stochastic wind forcing. *Geophys. Res. Lett.,* **39,** L11606, doi:10.1029/2012GL051684.

Panetta, R. L., 1993: Zonal jets in wide baroclinically unstable regions: Persistence and scale selection. *J. Atmos. Sci.,* **50,** 2073–2106, doi:10.1175/1520-0469(1993)050<2073: ZJIWBU>2.0.CO;2.

Pedlosky, J., 1984: The equations for geostrophic motion in the ocean. *J. Phys. Oceanogr.,* **14,** 448–455, doi:10.1175/ 1520-0485(1984)014<0448:TEFGMI>2.0.CO;2.

Polvani, L. M., J. C. McWilliams, M. A. Spall, and R. Ford, 1994: The coherent structures of shallow-water turbulence: Deformation-radius effects, cyclone/anticyclone asymmetry and gravity-wave generation. *Chaos,* **4,** 177–186, doi:10.1063/1.166002.

Radko, T., and M. E. Stern, 1999: On the propagation of oceanic mesoscale vortices. *J. Fluid Mech.,* **380,** 39–57, doi:10.1017/ S0022112098003371.

Rhines, P. B., 1975: Waves and turbulence on a beta-plane. *J. Fluid Mech.,* **69,** 417–443, doi:10.1017/S0022112075001504.

Richards, K. J., N. A. Maximenko, F. O. Bryan, and H. Sasaki, 2006: Zonal jets in the Pacific Ocean. *Geophys. Res. Lett.,* **33,** L03605, doi:10.1029/2005GL024645.

Risien, C. M., and D. B. Chelton, 2008: A global climatology of surface wind and wind stress fields from eight years of QuikSCAT scatterometer data. *J. Phys. Oceanogr.,* **38,** 2379–2413, doi:10.1175/2008JPO3881.1.

Ruppert-Felsot, J. E., O. Praud, E. Sharon, and H. L. Swinney, 2005: Extraction of coherent structures in a rotating turbulent flow experiment. *Phys. Review E,* **72,** 016311, doi:10.1103/ PhysRevE.72.016311.

Schlax, M. G., and D. B. Chelton, 2008: The influence of mesoscale eddies on the detection of quasi-zonal jets in the ocean. *Geophys. Res. Lett.,* **35,** L24602, doi:10.1029/2008GL035998.

——, ——, and M. H. Freilich, 2001: Sampling errors in wind fields constructed from single and tandem scatterometer datasets. *J. Atmos. Oceanic Technol.,* **18,** 1014–1036, doi:10.1175/ 1520-0426(2001)018<1014:SEIWFC>2.0.CO;2.

Srinivasan, K., and W. R. Young, 2012: Zonostrophic instability. *J. Atmos. Sci.,* **69,** 1633–1656, doi:10.1175/JAS-D-11-0200.1.

Storch, J. S. V., C. Eden, I. Fast, H. Haak, D. Hernández-Deckers, E. Maier-Reimer, J. Marotzke, and D. Stammer, 2012: An estimate of the Lorenz energy cycle for the world ocean based on the 1/10° STORM/NCEP simulation. *J. Phys. Oceanogr.,* **42,** 2185–2205, doi:10.1175/JPO-D-12-079.1.

Taguchi, B., R. Furue, N. Komori, A. Kuwano-Yoshida, M. Nonaka, H. Sasaki, and W. Ohfuchi, 2012: Deep oceanic zonal jets constrained by fine-scale wind stress curls in the South Pacific Ocean: A high-resolution coupled GCM study. *Geophys. Res. Lett.,* **39,** L08602, doi:10.1029/2012GL051248.

Tanaka, Y., and K. Akitomo, 2010: Alternating zonal flows in a two-layer wind-driven ocean. *J. Oceanogr.,* **66,** 475–487, doi:10.1007/s10872-010-0040-x.

Theiss, J., 2004: Equatorward energy cascade, critical latitude, and the predominance of cyclonic vortices in geostrophic turbulence. *J. Phys. Oceanogr.,* **34,** 1663–1678, doi:10.1175/ 1520-0485(2004)034<1663:EECCLA>2.0.CO;2.

Thompson, A. F., 2010: Jet formation and evolution in baroclinic turbulence with simple topography. *J. Phys. Oceanogr.,* **40,** 257–278, doi:10.1175/2009JPO4218.1.

Tulloch, R., J. Marshall, and K. S. Smith, 2009: Interpretation of the propagation of surface altimetric observations in terms of planetary waves and geostrophic turbulence. *J. Geophys. Res.,* **114,** C02005, doi:10.1029/2008JC005055.

——, ——, C. Hill, and K. S. Smith, 2011: Scales, growth rates, and spectral fluxes of baroclinic instability in the ocean. *J. Phys. Oceanogr.,* **41,** 1057–1076, doi:10.1175/2011JPO4404.1.

van Sebille, E., I. Kamenkovich, and J. K. Willis, 2011: Quasi-zonal jets in 3-D Argo data of the northeast Atlantic. *Geophys. Res. Lett.,* **38,** L02606, doi:10.1029/2010GL046267.

Wang, J., M. A. Spall, G. R. Flierl, and P. Malanotte-Rizzoli, 2013: Nonlinear radiating instability of a barotropic eastern boundary current. *J. Phys. Oceanogr.,* **43,** 1439–1452, doi:10.1175/JPO-D-12-0174.1.

Weiss, J., 1991: The dynamics of enstrophy transfer in two-dimensional hydrodynamics. *Physica D,* **48,** 273–294, doi:10.1016/0167-2789(91)90088-Q.

Williams, G. P., 1978: Planetary circulations: 1. Barotropic representation of Jovian and terrestrial turbulence. *J. Atmos. Sci.,* **35,** 1399–1426, doi:10.1175/1520-0469(1978)035<1399:PCBROJ>2.0.CO;2.

Wortham, C. J., 2013: A multi-dimensional spectral description of ocean variability with applications. Ph.D. thesis, Massachusetts Institute of Technology and Woods Hole Oceanographic Institution, 184 pp.

——, and C. Wunsch, 2014: A multidimensional spectral description of ocean variability. *J. Phys. Oceanogr.,* **44,** 944–966, doi:10.1175/JPO-D-13-0113.1.

Wunsch, C., 2009: The oceanic variability spectrum and transport trends. *Atmos.–Ocean,* **47,** 281–291, doi:10.3137/OC310.2009.

——, 2010: Toward a midlatitude ocean frequency–wavenumber spectral density and trend determination. *J. Phys. Oceanogr.,* **40,** 2264–2281, doi:10.1175/2010JPO4376.1.

——, 2011: The decadal mean ocean circulation and Sverdrup balance. *J. Mar. Res.,* **69,** 417–434, doi:10.1357/002224011798765303.

——, and P. Heimbach, 2013: Dynamically and kinematically consistent global ocean circulation and ice state estimates. *Ocean Circulation and Climate: A 21st Century Perspective,* 2nd ed., G. Siedler et al., Eds., Elsevier, 553–579.

Zhan, P., A. C. Subramanian, F. Yao, and I. Hoteit, 2014: Eddies in the Red Sea: A statistical and dynamical study. *J. Geophys. Res.,* **119,** 3909–3925, doi:10.1002/2013JC009563.